Title

Clonally expanded, targetable, natural killer-like NKG7 T cells seed the aged spinal cord to disrupt myeloid-dependent wound healing

Authors

Kong, Guiping

Song, Yayue

Yan, Yuyang

et al.

Publication Date

2025

DOI

10.1016/j.neuron.2024.12.012

Neuron

Article

Clonally expanded, targetable, natural killer-like NKG7 T cells seed the aged spinal cord to disrupt myeloid-dependent wound healing

Graphical abstract

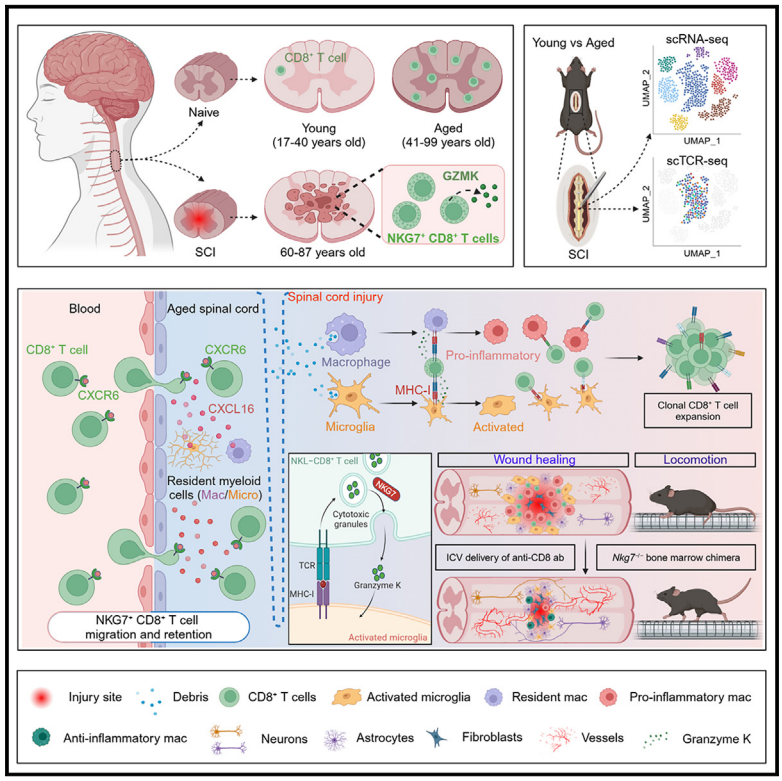

Highlights

- Natural killer-like NKG7 T cells seed the spinal cord of aged individuals and mice
- NKLT cells accumulate in the spinal cord via a CXCR6-CXCL16 axis
- NKG7 T cells interact with myeloid cells to clonally expand, disrupting wound healing
- NKG7 deletion or CD8 T cell neutralization promotes wound healing and recovery

Authors

Guiping Kong, Yayue Song, Yuyang Yan, ..., Christian R. Engwerda, Luming Zhou, Simone Di Giovanni

Correspondence

l.zhou13@imperial.ac.uk (L.Z.), s.di-giovanni@imperial.ac.uk (S.D.G.)

In brief

Kong et al. report that, during aging, cytotoxic T cells accumulate and clonally expand in the spinal cord of individuals and mice, where they exacerbate tissue damage after injury by disrupting myeloid-cell-mediated wound healing. This mechanism can be neutralized by monoclonal antibodies that promote tissue repair and neurological recovery.

Kong et al., 2025, Neuron *113*, 1–17
March 5, 2025
https://doi.org/10.1016/j.neuron.2024.12.012

CellPress

Neuron

CellPress
OPEN ACCESS

Article

Clonally expanded, targetable, natural killer-like NKG7 T cells seed the aged spinal cord to disrupt myeloid-dependent wound healing

Guiping Kong,[1] Yayue Song,[1] Yuyang Yan,[1] Samantha M. Calderazzo,[3,14] Madhu Sudhana Saddala,[4] Fabian De Labastida Rivera,[5] Jonathan D. Cherry,[3,14] Noah Eckman,[6,15,16,17,18,19] Eric A. Appel,[6,15,16,17,18,19] Adam Velenosi,[7,8] Vivek Swarup,[4] Riki Kawaguchi,[9,10] Susanna S. Ng,[5,11] Brian K. Kwon,[7,12] David Gate,[13] Christian R. Engwerda,[5] Luming Zhou,[1,2,*] and Simone Di Giovanni[1,20,*]

[1]Molecular Neuroregeneration, Division of Neuroscience, Department of Brain Sciences, Imperial College London, London, UK
[2]Precision Research Center for Refractory Diseases, Shanghai General Hospital, Shanghai Jiao Tong University School of Medicine, Shanghai 201620, China
[3]Department of Pathology and Laboratory Medicine, Boston University Chobanian & Avedisian School of Medicine, Boston, MA, USA
[4]Department of Neurobiology and Behaviour, School of Biological Sciences, University of California Irvine, Irvine, CA, USA
[5]QIMR Berghofer Medical Research Institute, Brisbane, QLD, Australia
[6]Department of Chemical Engineering, Stanford University, Stanford, CA, USA
[7]International Collaboration on Repair Discoveries, University of British Columbia, Vancouver, BC, Canada
[8]Praxis Spinal Cord Institute, Vancouver, BC, Canada
[9]Program in Neurogenetics, Department of Neurology, David Geffen School of Medicine, University of California, Los Angeles, Los Angeles, CA, USA
[10]Semel Institute for Neuroscience and Human Behaviour, David Geffen School of Medicine, University of California, Los Angeles, Los Angeles, CA, USA
[11]Institute of Experimental Oncology, Medical Faculty, University Hospital Bonn, University of Bonn, Bonn, Germany
[12]Department of Orthopaedics, University of British Columbia, Vancouver, BC, Canada
[13]The Ken & Ruth Davee Department of Neurology, Northwestern University Feinberg School of Medicine, Chicago, IL, USA
[14]Boston University Alzheimer's Disease and CTE Centers, Boston University Chobanian & Avedisian School of Medicine, Boston, MA, USA
[15]Department of Materials Science & Engineering, Stanford University, Stanford, CA, USA
[16]Department of Bioengineering, Stanford University, Stanford, CA, USA
[17]Department of Paediatrics, Endocrinology, Stanford University, Stanford, CA, USA
[18]ChEM-H Institute, Stanford University, Stanford, CA, USA
[19]Woods Institute for the Environment, Stanford University, Stanford, CA, USA
[20]Lead contact
*Correspondence: l.zhou13@imperial.ac.uk (L.Z.), s.di-giovanni@imperial.ac.uk (S.D.G.)
https://doi.org/10.1016/j.neuron.2024.12.012

SUMMARY

Spinal cord injury (SCI) increasingly affects aged individuals, where functional impairment and mortality are highest. However, the aging-dependent mechanisms underpinning tissue damage remain elusive. Here, we find that natural killer-like T (NKLT) cells seed the intact aged human and murine spinal cord and multiply further after injury. NKLT cells accumulate in the spinal cord via C-X-C motif chemokine receptor 6 and ligand 16 signaling to clonally expand by engaging with major histocompatibility complex (MHC)-I-expressing myeloid cells. NKLT cells expressing natural killer cell granule protein 7 (*Nkg7*) disrupt myeloid-cell-dependent wound healing in the aged injured cord. *Nkg7* deletion in mice curbs NKLT cell degranulation to normalize the myeloid cell phenotype, thus promoting tissue repair and axonal integrity. Monoclonal antibodies neutralizing $CD8^+$ T cells after SCI enhance neurological recovery by promoting wound healing. Our results unveil a reversible role for $NKG7^+CD8^+$ NKLT cells in exacerbating tissue damage, suggesting a clinically relevant treatment for SCI.

INTRODUCTION

While most demographic data indicate that spinal cord injury (SCI) affects mainly young males, with average age at the time of injury being in their forties,[1] SCIs have been occurring at an increasing rate in the expanding aging population.[2,3] The mammalian CNS has a limited ability to self-repair that further declines with aging, where mortality and functional impairment

Please cite this article in press as: Kong et al., Clonally expanded, targetable, natural killer-like NKG7 T cells seed the aged spinal cord to disrupt myeloid-dependent wound healing, Neuron (2024), https://doi.org/10.1016/j.neuron.2024.12.012

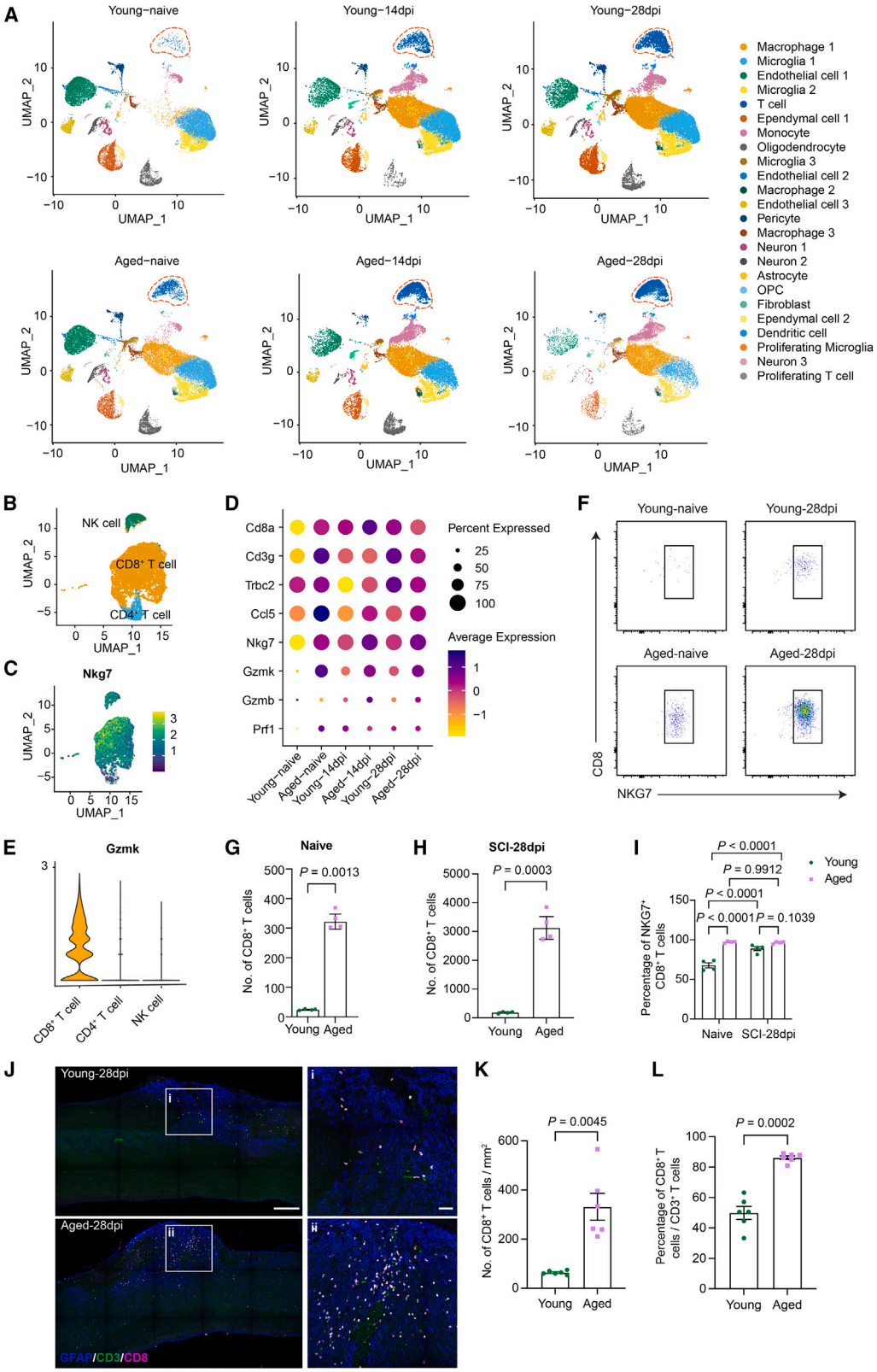

(legend on next page)

Please cite this article in press as: Kong et al., Clonally expanded, targetable, natural killer-like NKG7 T cells seed the aged spinal cord to disrupt myeloid-dependent wound healing, Neuron (2024), https://doi.org/10.1016/j.neuron.2024.12.012

are especially challenging.[4–7] However, the molecular and cellular mechanisms underpinning failure to repair and regenerate after CNS injury across the lifespan remain inadequately understood.

To date, regenerative failure after spinal injury has been attributed to two main factors: (1) the formation of a glia inhibitory environment that promotes growth cone collapse and (2) the lack of a neuronal regenerative response in long-projecting sensory and motor tracts.[8] Experimental evidence suggests that providing a favorable glial environment along with the activation of the otherwise limited intrinsic potential of neurons to sprout and regenerate axons may maximize repair.[1] However, rarely are studies conducted across the lifespan. As an exception, a previous report showed that neuronal deletion of phosphatase and tensin homolog (*Pten*) partially limits the aging-dependent axonal regenerative decline of corticospinal tracts in mice.[4,5]

In addition to astrocytes and myelin proteins, myeloid and innate immune cells have been shown to play a prominent role in the tissue injury response and wound healing after SCI.[3,7] Notably, the impact of adaptive immune B and T cells on spinal cord wound healing, plasticity, and regeneration is less well defined and remains controversial.[9–13] While it is clear that immune cells interact with glial and vascular cells after experimental SCI, as shown in recent studies,[10] it has been suggested that temporal and spatial control of T cell discrete subpopulations may be needed to favor repair after SCI.[14,15] Additionally, it has been shown that immunization with myelin basic protein can promote recovery from spinal cord contusion.[16]

In addition to the more classical role of parenchymal lymphocytes, interestingly, a role for meningeal type 2 innate lymphocytes in promoting recovery after SCI has been proposed.[17]

Historically, most experimental SCI studies have been conducted in young animals. Yet, these models do not consider age as an important factor affecting repair and recovery in clinical SCI. Thus, a better understanding of age-associated changes to SCI could allow for the identification of strategies to promote repair and recovery in human SCI.

As an exception to the paucity of the available studies, examination of myelin pathology revealed that aged rats had a significantly higher degree of tissue damage and demyelination, as well as reduced remyelination as compared with young rats following contusion SCI. However, how immunity might contribute to the phenotype was not investigated.[18] A recent study showed that compared with the young, aged mice had blunted myeloid responses affecting repair after SCI and revealed communication between myeloid cells in the spinal cord and lymphatic endothelial cells in the meninges, possibly supporting vascular repair.[19]

Here, we hypothesized that changes to the molecular and cellular signatures of the spinal cord microenvironment across the lifespan might affect wound healing, axonal injury responses, and functional recovery. To test this hypothesis, we investigated the molecular and cellular signatures associated with the wound-healing response after an experimental SCI in the mouse across the lifespan.

To this end, we initially conducted single-cell RNA sequencing (scRNA-seq) experiments from the spinal cord of young and aged mice preceding and following SCI. This allowed identifying an aging and injury-dependent enrichment in hyperexpanded and hyperactive $CD8^+$ T cells with signatures typical of natural killer (NK)-like T (NKLT) cells. Specifically, these cells had heightened expression of NK cell granule protein 7 (NKG7) and granzyme K (GZMK). Mechanistically, we found that the aging-dependent accumulation of cytotoxic NKLT cells within the spinal cord relies on a C-X-C motif chemokine ligand 16 (CXCL16)-C-X-C motif chemokine receptor 6 (CXCR6) axis. We detected that CXCL16 is mainly expressed by the myeloid cells, such as macrophages/microglia, and CXCR6 is selectively expressed by T cells.

Surprisingly, NKLT cells are also found in the intact and injured human spinal cord. Remarkably, NKLT cells clonally expand in the aged spinal cord and after injury. $NKG7^+CD8^+$ NKLT cells exacerbate tissue injury by degranulating GZMK in proximity to major histocompatibility complex (MHC)-I-expressing macrophages/microglia to disrupt their wound-healing properties. The cytotoxicity of NKTL cells requires *Nkg7*, and its deletion promotes wound healing and preserves axonal integrity in mice. Lastly, monoclonal antibodies against $CD8^+$ T cells significantly limit axonal retraction and promote wound healing and neurological recovery.

Altogether, we reveal a novel, reversible, age-dependent cellular mechanism by which clonally expanded NKLT cells restrict wound healing and repair after SCI. These data also propose CNS antibody-mediated depletion of cytotoxic $CD8^+$ NKLT cells as a clinically suitable intervention to promote repair after SCI.

Figure 1. Analysis of scRNA-seq in the spinal cord of naive and injured young and aged mice

(A) Uniform manifold approximation and projection (UMAP) plots of the cells collected from naive and injured spinal cord at 14 and 28 days post injury (dpi) from young and aged mice (n = 3 biological replicates in each group). Cell types are color coded and annotated based on the canonical marker genes listed in Figure S2. Red dashed line circle labels T cell cluster.

(B and C) UMAP plots of $CD8^+$ T cell, $CD4^+$ T cell, and NK cell clusters from isolated T cell population (B) and the expression pattern of *Nkg7* in each T cell subcluster (C). Expression values are log-normalized counts.

(D) Dot plot of $CD8^+$ T cell marker genes and age-dependent differentially expressed genes in naive and injured spinal cord. The color of the dots represents the average expression level. The size of the dots represents the percentage of cells with at least one unique molecular identifier (UMI) detected per gene.

(E) VlnPlot using scCustomize package shows the expression levels of *Gzmk* among T cell subtypes from scRNA-seq analysis.

(F) Representative flow cytometry plots show the $NKG7^+CD8^+$ T cell populations in the mouse spinal cord in different conditions.

(G–I) Quantification of the number of $CD8^+$ T cells and the percentage of $NKG7^+CD8^+$ T cells of (F) (n = 4 biological replicates).

(J) Representative immunostaining images of spinal cord sagittal sections showing $CD8^+$ T cells at the lesion site of young and aged mice 28 days after SCI.

(K and L) Quantification of density (K) and percentage (L) of $CD8^+$ T cells at the lesion site of young versus aged mice 28 days after SCI (n = 6 biological replicates). Unpaired two-sided t test with Welch's correction (G, H, K, and L). Two-way ANOVA followed by post hoc Tukey's test (I). Data are means ± SEM (G–I, K, and L). Scale bars: 100 μm (low magnification in J), 20 μm (high magnification in J).

Please cite this article in press as: Kong et al., Clonally expanded, targetable, natural killer-like NKG7 T cells seed the aged spinal cord to disrupt myeloid-dependent wound healing, Neuron (2024), https://doi.org/10.1016/j.neuron.2024.12.012

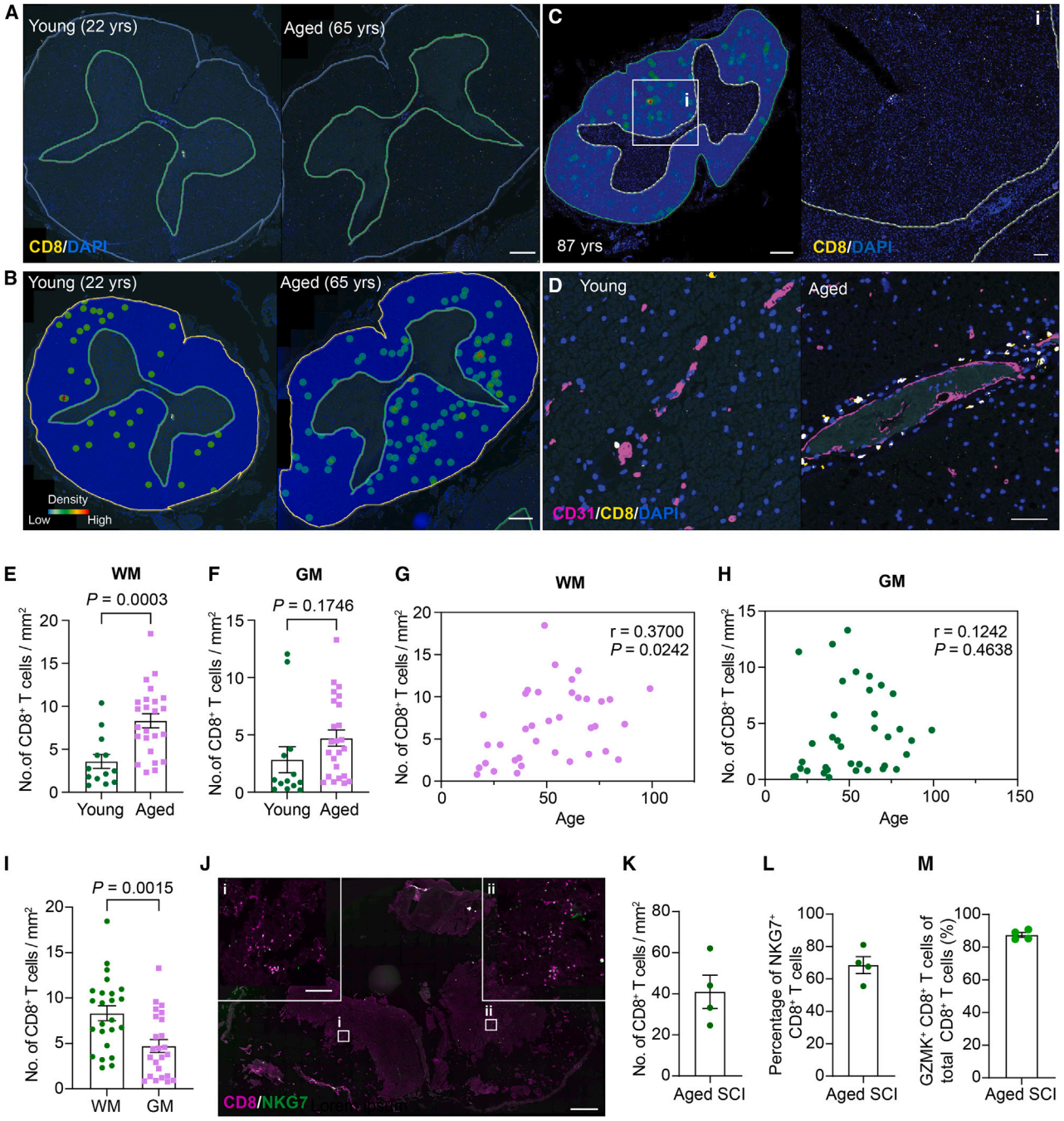

Figure 2. Analysis of CD8$^+$ T cells in both naive and injured human spinal cord

(A) Representative immunostaining images of the heatmap in (B).

(B) Representative heatmap of CD8$^+$ T cell distribution in the white matter (WM) of the spinal cord in young and aged human subjects generated by HALO software.

(C) Representative image of WM CD8$^+$ T cell distribution in aged naive spinal cord (87 years).

(D) Representative image of WM perivascular CD8$^+$ T cell distribution with age.

(E and F) Quantification of CD8$^+$ T cells in the WM (E) and gray matter (GM) (F) of young versus aged naive human spinal cord (n = 13 and 24 biological replicates for young and aged groups, respectively).

(G and H) Correlation assessments between the number of CD8$^+$ T cells and age in the WM (G) and GM (H) of human spinal cord (n = 13 and 24 biological replicates for young and aged groups, respectively).

(legend continued on next page)

RESULTS

Cytotoxic NKG7$^+$CD8$^+$ NKLT cells accumulate in the spinal cord preceding and following an injury across the lifespan via CXCL16-CXCR6 signaling

We initially assessed axonal retraction of dorsal root ganglia sensory and corticospinal motor axons as well as neurological recovery in 2- to 3- and 20- to 22-month-old mice in a model of spinal cord dorsal hemisection (Figure S1A). In line with previous evidence,[20] axonal retraction of both sensory and motor axons was significantly more pronounced in aged mice (Figures S1B and S1C), as was the fibrosis (Figures S1D and S1E). Next, we investigated the cellular and molecular signatures associated with aging and injury in the mouse spinal cord by scRNA-seq in naive 2- to 3- or 20- to 22-month-old mice at 14 and 28 days post SCI (Figure S2A). These time points were selected because they correspond to when wound healing starts establishing and consolidating, respectively.[21–23] After quality control, cells were assigned to 24 main cell types according to canonical marker genes (Figure S2B). Surprisingly, multidimensional reduction of scRNA-seq data revealed that T cells, mostly CD8, were enriched in the aged spinal cord before and after SCI (Figures 1A, 1B, and S3). Given their age- and injury-dependent modulation and the poor understanding of their role after SCI, subsequent experiments focused on unraveling the identity and function of T cells in tissue damage and repair. In addition to genes encoding pan-T cell markers CD3 and T cell receptor (TCR), cytotoxic hallmarks of this aged CD8$^+$ T cell population included *Nkg7*, CC motif chemokine ligand 5 (*Ccl5*), and *Gzmk* (Figures 1C–1E; Table S1). Flow cytometry confirmed the striking increase in the number of CD8$^+$ T cells in the aged spinal cord as well as post SCI, while CD4$^+$ T cells represented a much smaller population (Figures 1F–1H, S4, S5A, and S5B). Flow cytometry data showed a high percentage of NKG7$^+$CD8$^+$ T cells in both naive and injured spinal cords of the aged mice (Figures 1I and S5C). A higher level of GZMK was observed in aged CD8$^+$ T cells in the spinal cord after injury compared with young (Figures S5D and S5E). Although *Nkg7* is also expressed in NK cells and $\gamma\delta$ T cells, single-cell and flow cytometry analysis confirmed that these two cell populations are extremely scarce in the spinal cord (Figure S6), supporting a role of *Nkg7* in CD8$^+$ T cells in the aged and injured cord. Further, these CD8$^+$ T cells expressed low levels of classical NK, senescence, and tissue residency markers as well as intermediate levels of T effector memory genes (Figures S7A–S7C). However, they expressed high levels of *Pdcd1* and *Ctla4*, suggesting an exhausted phenotype (Figure S7B). Importantly, while they had low expression of *Cxcr3* and *Cxcr4*, they expressed high levels of the T cell migration and retention marker *Cxcr6* (Figure S7D). Notably, CD8$^+$ T cells were found mainly located in the white matter of naive mouse spinal cord (Figure S8D) and accumulated within the injury site after SCI in both young and aged mice, with a more significant increase in aged animals (Figures 1J–1L and S8A–S8C).

An age-dependent increase of CD8$^+$ T cells was also found in the white matter of the healthy human spinal cord (Figures 2A–2C and 2E–2I), where they were enriched in proximity to the perivascular compartment (Figures 2D and S9A). Importantly, cytotoxic NKG7$^+$CD8$^+$ T cells and GZMK were also located in proximity to the spinal cord lesion site in SCI patients (Figures 2J–2M and S9B).

The expression of Cxcr6 in CD8$^+$ T cells that increases with age and after injury in young animals was paralleled by the expression of the CXCR6 ligand *Cxcl16*, predominantly in macrophages/microglia (Figures 3A and 3B). Flow cytometry confirmed the age- and injury-dependent preferential increase in the number of CD8$^+$ T cells compared with CD4$^+$ T cells both in the peripheral blood and spinal cord; importantly, CD8$^+$ T cells express CXCR6 (Figures 3C–3H). This implied a CXCL16-CXCR6 axis for CD8$^+$ T cell accumulation into the spinal cord that was experimentally validated. We investigated this signaling axis by using CXCL16 antagonizing antibodies delivered via osmotic minipums into the cerebrospinal fluid from 1 h until 2 weeks after injury. CXCL16 antagonism resulted in a significant decrease of CD8$^+$ T cells in the spinal cord (Figures 3I–3K), providing evidence for a CXCL16-dependent accumulation of CD8$^+$ T cells into the spinal cord.

Next, to investigate whether aged CD8$^+$ T cells communicate with the cellular environment of the injured spinal cord, the scRNA-seq dataset was interrogated for cell-cell communication by CellChat. This suggested stronger interactions between T cells and activated macrophages/microglia compared with other cell types, although some level of interaction was also observed in endothelial cells in the aged mice 28 days post injury (Figures 4A and 4B). Importantly, similar interaction patterns occurred in both young and aged mice after injury; however, these were more pronounced in the aged (Figures S10 and S11). In support of this, co-immunofluorescence experiments in young and aged mice showed the highest number of CD8$^+$ T cells expressing GZMK in close proximity to ionized calcium-binding adaptor molecule 1-positive (Iba1$^+$) myeloid cells in the aged injured spinal cord (Figures 4C and 4D). Importantly, Iba1$^+$ cells displayed an age-dependent increase in expression of MHC-I, which is recognized by TCRs on CD8$^+$ T cells (Figures S12A and S12B). Iba1$^+$ cells also showed a dramatic age-dependent shift toward shorter and fewer branches after SCI (Figures 4E and 4F), implying their activation.

Antigen-activated CD8$^+$ T cells exacerbate spinal cord tissue damage

Next, we investigated whether antigenic activation of CD8$^+$ T cells within the injured spinal cord would exacerbate tissue damage and affect the phenotype of Iba1$^+$ injury-activated

(I) Quantification of CD8$^+$ T cells in gray and white matter of aged human spinal cord.
(J–L) Immunostaining data show the expression of NKG7 in CD8$^+$ T cells at the injury site of aged human spinal cord (n = 4 biological replicates).
(M) Quantification of GZMK$^+$CD8$^+$ T cells at the lesion site of the injured human spinal cord (n = 4 biological replicates, within 3 mm from lesion epicenter).
Unpaired two-sided t test with Welch's correction (E, F, and I). Two-tailed Pearson's correlation test (G and H). Data are means ± SEM (E, F, I, and K–M). Scale bars: 1,000 μm (A, B, low magnification in C, and low magnification in J), 250 μm (high magnification in C), and 50 μm (D and high magnification in J).

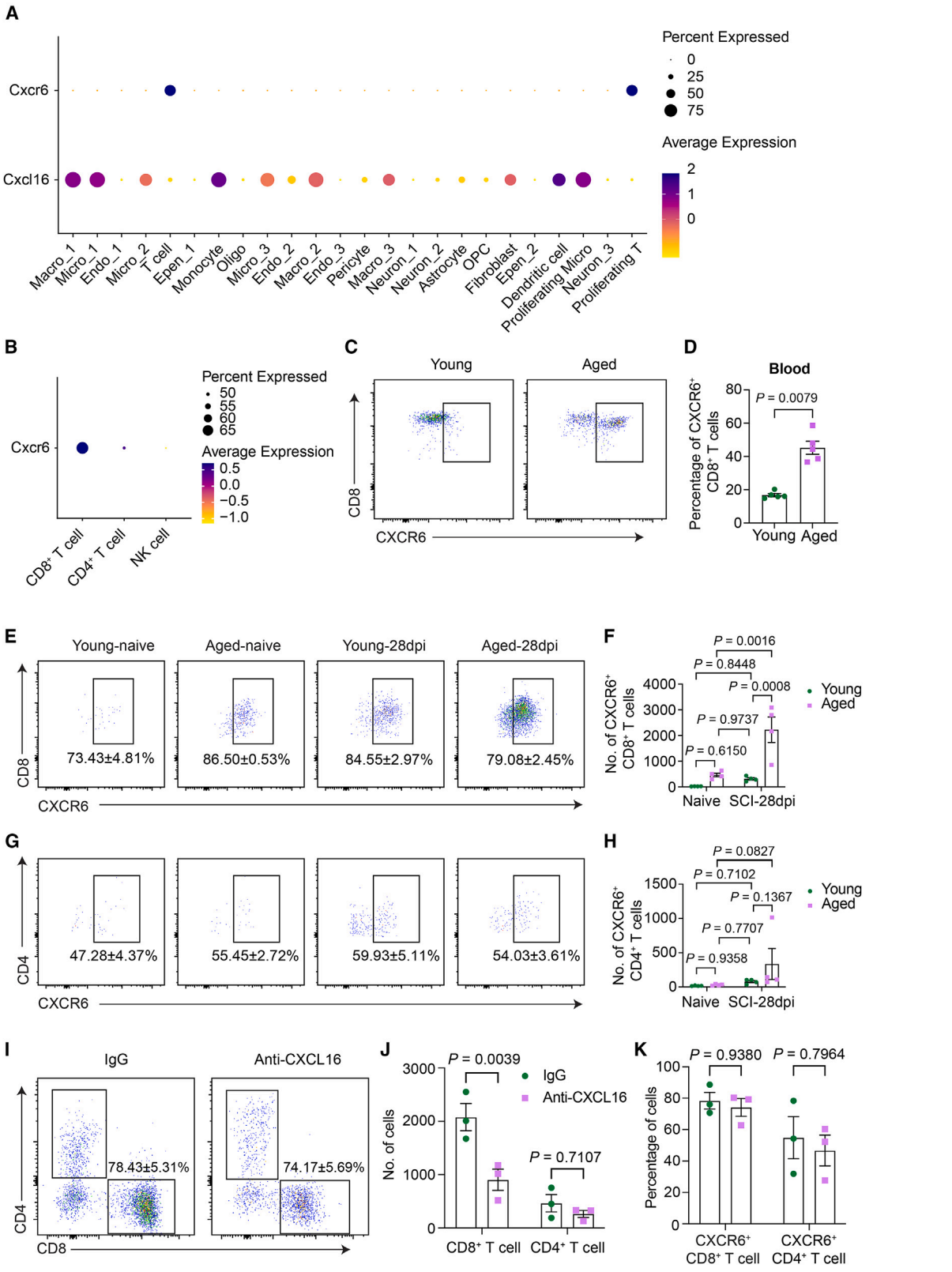

(legend on next page)

macrophage/microglia (IAM). We utilized adult OT-I *Rag2*$^{-/-}$ mice to allow activation of CD8$^+$ T cells exclusively after ovalbumin antigen stimulation on a T cell null background. Ovalbumin peptide (SIINFEKL) or PBS was injected into the SCI site 7 days post injury (Figure S13A). Flow cytometry showed the expected activation of CD8$^+$ T cells (Figures S13B and S13C) and a high proliferation rate for CD8$^+$ T cells between 1 and 7 days, with a peak at 3 days when the ovalbumin peptide was presented by myeloid cells (Figures S13D–S13F). Notably, activation of CD8$^+$ T cells did not cause tissue damage in the naive spinal cord (Figure S14A). However, activation of CD8$^+$ T cells after SCI exacerbated tissue fibrosis, reduced branching of Iba1$^+$ cells, and axons were found to terminate further away from the spinal lesion compared with control (Figures 4G–4L, S14B, and S14C).

Cytotoxic NKG7$^+$CD8$^+$ NKLT cells exhibit age- and injury-dependent clonal expansion

When TCRs on the surface of CD8$^+$ T cells recognize antigens presented by MHC-I, they clonally expand. Thus, single-cell TCR sequencing (scTCR-seq) was carried out to assess whether NKG7$^+$CD8$^+$ T cells display an age- and injury-dependent antigen-specific response (Figure 5A). Remarkably, data analysis revealed a very prominent clonal expansion of CD8$^+$ T cells in the aged naive as well as in the young and aged spinal cord after injury, where clonal expansion was highest (Figures 5B–5F and S15; Table S2). Clonally expanded CD8$^+$ T cells showed a hyperactivity gene expression profile, including high expression of *Nkg7*, *Ccl5*, and *Gzmk*, and the exhaustion and tissue retention markers *Pdcd1*, *Tigit*, and *Cxcr6* (Figure 5G; Table S3). These results suggest that exhausted CD8$^+$ T cells respond to antigens to mount a cytotoxic immune response. Strikingly, gene expression analysis of *Nkg7* showed a positive correlation with CD8$^+$ T cell clonal expansion (Figure 5H).

Since TCR sequencing showed that NKG7$^+$CD8$^+$ T cells were clonally hyperexpanded as a function of age and injury, we next investigated whether aging and/or antigen stimulation would lead to clonal expansion of NKG7$^+$CD8$^+$ T cells. We measured clonal expansion by flow cytometry and proliferation assays after antigen stimulation. Flow cytometry showed a significant increase in NKG7$^+$CD8$^+$ T cells in the aged peripheral blood (Figures 6A–6C), and clonal cell proliferation assays revealed antigen-dependent clonal expansion and increase in NKG7$^+$CD8$^+$ T cells and in NKG7 expression levels (Figures 6D–6F). Further, CellChat analysis showed higher communication probability in MHC-I signaling network and increased interaction strength with myeloid cells of clonally hyperexpanded CD8$^+$ T cell compared with CD8$^+$ T cells with single clones (Figures S16A–S16C).

Regulation of *Nkg7* expression in CD8$^+$ T cells requires phosphorylated STAT3 (p-STAT3)

In order to identify putative transcription factors (TFs) that are involved in *Nkg7* expression in CD8$^+$ T cells, we interrogated the Gene Transcription Regulation Database (GTRD) to predict which TFs bind to the Nkg7 promoter. Among the predicted TFs (Table S4), four TFs, including *Eomes*, *Stat3*, *Runx1*, and *Runx2*, were found to be differentially expressed in CD8$^+$ T cells as a function of age and injury in the spinal cord in our scRNA-seq data and were therefore selected for further investigation (Table S5). In particular, *Stat3* showed very significant upregulation in aged CD8$^+$ T cells in both naive and injured spinal cords (Figure 6G). We next treated primary CD8$^+$ T cells with inhibitors for STAT3, RUNX1, RUNX2, and RUNX agonist for 5 days, followed by reverse-transcription polymerase chain reaction (RT-PCR) for *Nkg7*. Interestingly, only inhibition of p-STAT3 significantly reduced *Nkg7* expression in CD8$^+$ T cells (Figure 6H). Immunostaining confirmed that p-STAT3 is expressed in CD8$^+$ T cells in the lesion site of the aged spinal cord (Figures 6I and 6J). Next, we employed bone marrow chimeras (BMCs) by using *Nkg7* reporter mice (*Nkg7*-cre × mT/mG, NKG7$^+$/GFP$^+$ versus NKG7$^-$/TdT$^+$ cells) that we previously described[24] and that allow detection of NKG7 protein expression in the absence of suitable antibodies for immunofluorescence in mice. SCI was carried out in aged 22-month-old *Nkg7*-cre × mT/mG bone-marrow-reconstituted animals. Next, the p-STAT3 inhibitor S3I-201 or vehicle was delivered systemically i.p. 3 times/week from day 1 until sacrifice at day 14. Importantly, S3I-201 delivery showed reduced p-STAT3 expression levels in CD8$^+$ T cells and led to a reduction in the percentage of NKG7$^+$/GFP$^+$ CD8$^+$ T versus NKG7$^-$/TdT$^+$ cells in both blood and spinal cord after SCI (Figures 6K–6P and S17A–S17C).

Altogether, aging and SCI lead to NKG7$^+$CD8$^+$ T cell clonal expansion. Further, NKG7 is induced by aging and antigen stimulation and is highly expressed in clonally expanded CD8$^+$ T cells, where its expression is regulated by p-STAT3.

Nkg7 deletion attenuates activation of IAM and promotes tissue repair

Next, we investigated whether *Nkg7* deletion would promote wound healing after SCI by utilizing BMCs. As previously published,[24] a floxed *Nkg7* mouse line was created and crossed

Figure 3. Aging-dependent spinal cord retention of CD8$^+$ T cells is regulated by CXCL16-CXCR6 axis

(A) Dot plot shows the expression levels of *Cxcr6* and *Cxcl16* in each cell type in the spinal cord.

(B) Dot plot shows the dominant expression of *Cxcr6* in CD8$^+$ T cells.

(C and D) Representative flow cytometry plots (C) and quantification (D) of CXCR6$^+$ CD8$^+$ T cells in the blood of young and aged mice (n = 5 biological replicates in each group).

(E and F) Representative flow cytometry plots (E) and quantification (F) of CXCR6$^+$ CD8$^+$ T cells in naive spinal cord and spinal cord lesion site in young and aged mice (n = 4 biological replicates in each group).

(G and H) Representative flow cytometry plots (G) and quantification (H) of CXCR6$^+$ CD4$^+$ T cells in naive spinal cord and spinal cord lesion site in young and aged mice (n = 4 biological replicates in each group).

(I–K) Representative flow cytometry plots (I) and quantification (J and K) of CD8$^+$ and CD4$^+$ T cells at the spinal cord lesion site in aged mice 2 weeks after SCI and IgG or CXCL16 antagonism (n = 3 biological replicates in each group).

Unpaired two-tailed t test with Welch's correction (D), two-way ANOVA followed by post hoc Tukey's test (F and H). Two-way ANOVA followed by post hoc Sidak's test (J and K). Data are means ± SEM (D, F, H, J, and K).

Please cite this article in press as: Kong et al., Clonally expanded, targetable, natural killer-like NKG7 T cells seed the aged spinal cord to disrupt myeloid-dependent wound healing, Neuron (2024), https://doi.org/10.1016/j.neuron.2024.12.012

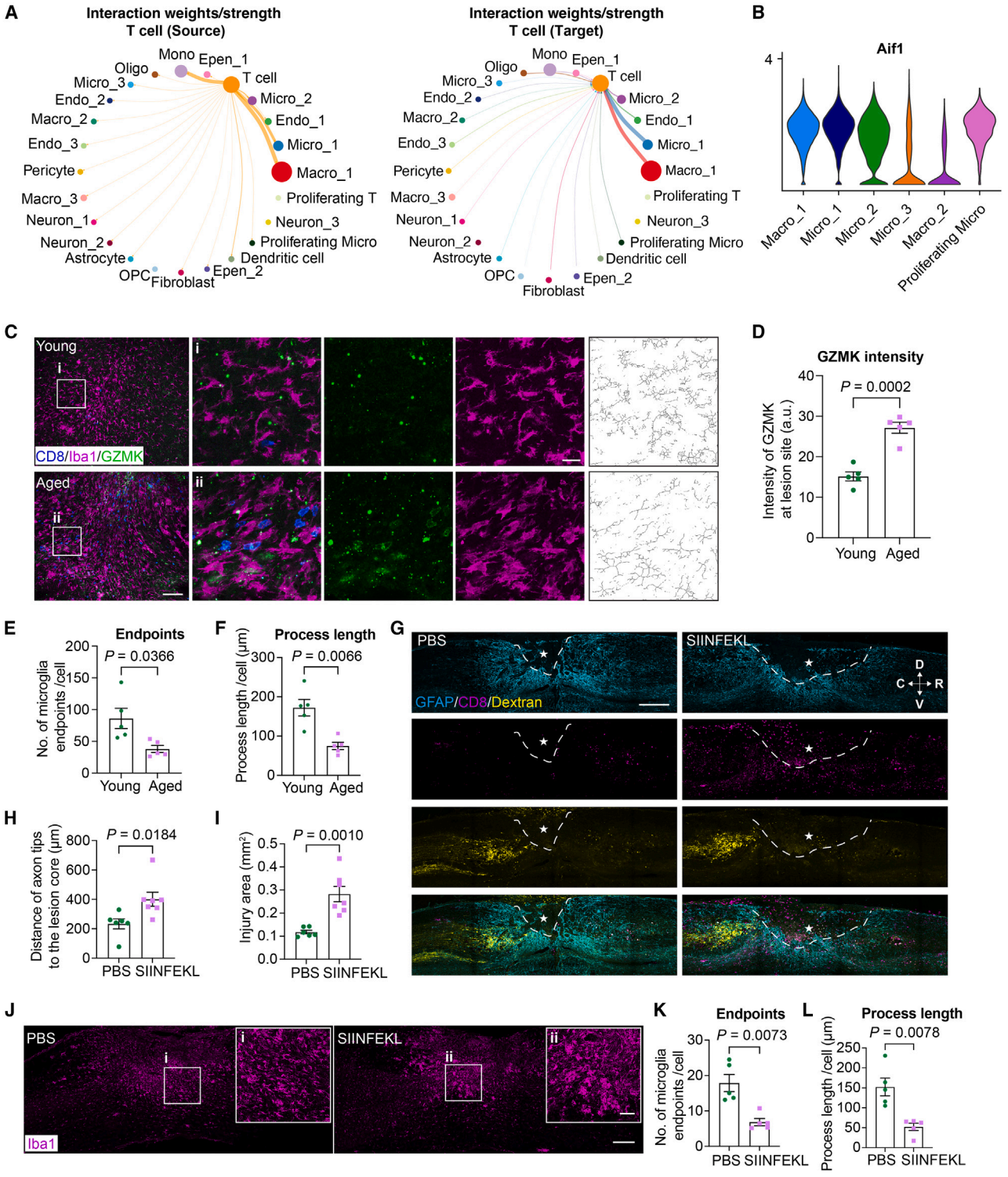

Figure 4. Activated CD8⁺ T cells interact with myeloid cells after SCI

(A and B) CellChat analysis of the interactions between T cells and other cell types in the aged 28 days post injury group of scRNA-seq data showing the preferential interaction between T cells and macrophage/microglia (A) that are Iba1⁺ (B). Dot size in the circle plots of (A) indicates the group size, and edge weight indicates the interaction strength.

(C) Representative images of the lesion site on sagittal spinal cord sections immunostained with CD8, Iba1, and granzyme K (GZMK) in young and aged mice 28 days after SCI. High-magnification images of Iba1 staining are converted to skeleton images showing the ramification of Iba1⁺ cells.

(legend continued on next page)

Please cite this article in press as: Kong et al., Clonally expanded, targetable, natural killer-like NKG7 T cells seed the aged spinal cord to disrupt myeloid-dependent wound healing, Neuron (2024), https://doi.org/10.1016/j.neuron.2024.12.012

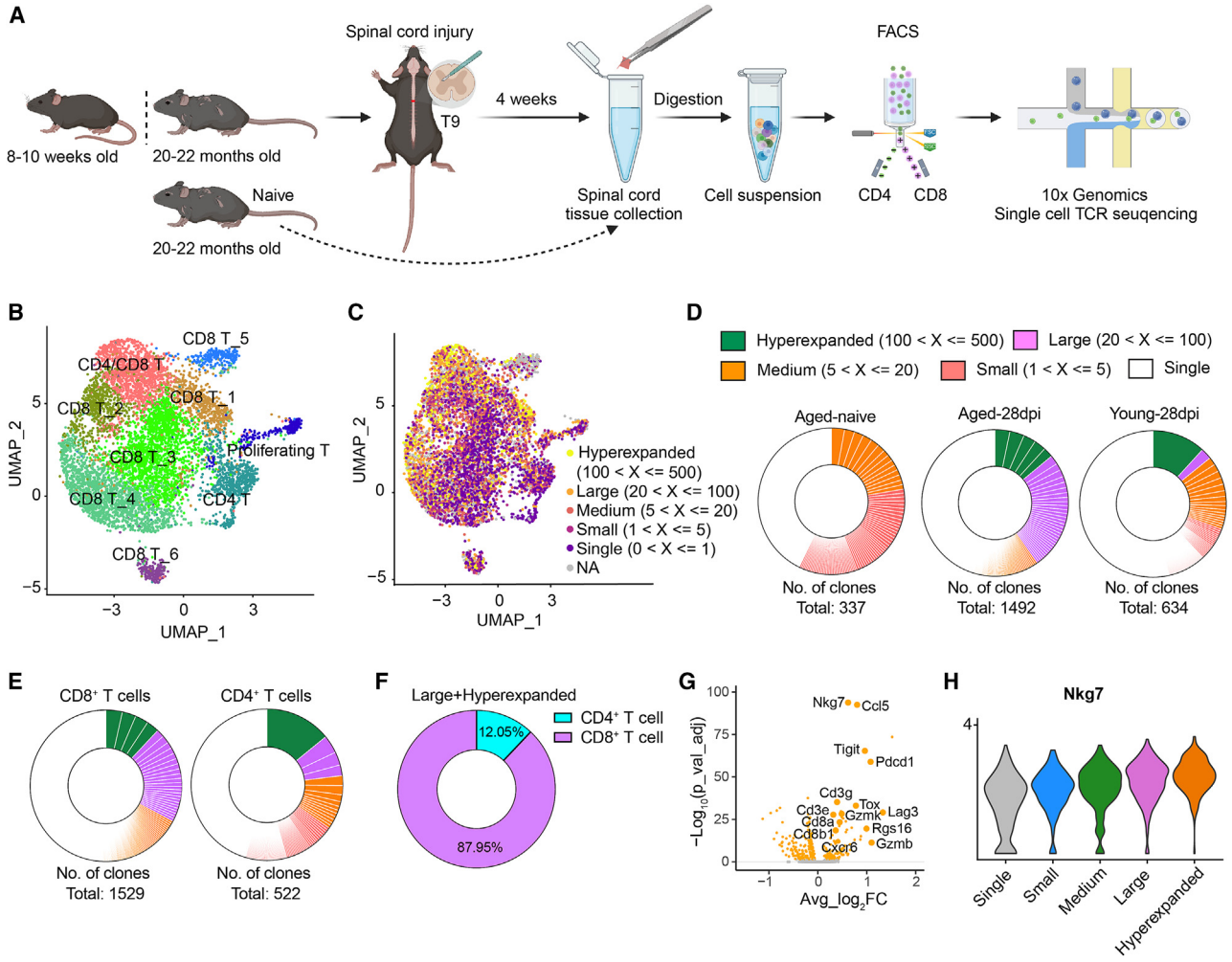

Figure 5. Clonal expansion of CD8⁺ T cells in the aged and injured spinal cord

(A) Workflow diagram of CD8⁺ and CD4⁺ T cell sorting from naive aged spinal cord, injury site of young and aged spinal cord 28 days post injury (dpi) followed by TCR scRNA-seq.

(B and C) UMAP plot of CD8⁺ and CD4⁺ subtypes (B) and TCR clones (C) (n = 4 biological replicates in each group).

(D) Representative plots of TCR clones in naive aged, injured young, and aged spinal cord showing age- and injury-dependent clonal expansion.

(E and F) CD8⁺ versus CD4⁺ T cell clones (E) and quantification of large and hyperexpanded clones (F) showing age- and injury-dependent predominance of CD8⁺ T cell clonal expansion.

(G) Volcano plot shows differentially expressed (DE) genes in clonally expanded versus single clones of CD8⁺ T cells.

(H) VlnPlot shows *Nkg7* expression changes in CD8⁺ T cells with clonal expansion.

Wilcox rank-sum tests (G).

onto a lck-cre line (lymphocyte-specific protein tyrosine kinase). Therefore, in our BMCs, *Nkg7* was specifically deleted in T cells. Bone marrow from *Nkg7*$^{-/-}$ mice was transferred into irradiated wild-type (WT) mice (Figure 7A). Next, SCI was carried out in aged WT or *Nkg7*$^{-/-}$ bone-marrow-reconstituted animals, which were sacrificed 12 weeks post injury (Figure 7A). *Nkg7* deletion

(D–F) Quantification of GZMK intensity (D), number of endpoints of Iba1⁺ cell branching (E), and process length (F) at the spinal cord lesion site in young and aged mice (n = 5 biological replicates).

(G) Representative images of sagittal sections of spinal cord with dextran-labeled dorsal column axons and co-stained with GFAP and CD8 in PBS- or SIINFEKL-stimulated young OT-I *Rag2*$^{-/-}$ mice 14 days after SCI. The dash lines indicate the lesion border. Asterisks indicate the lesion center.

(H and I) Quantification of distance of axon tips from the lesion core (H) and injury area (I) (n = 6 and 7 of spinal cord for PBS and SIINFKEL groups, respectively).

(J–L) Representative images of Iba1-immunostained sagittal sections of spinal cord lesion site (J) and quantification of endpoints number (K) and process length (L) of Iba1⁺ cells (n = 5 biological replicates).

Unpaired two-sided t test with Welch's correction (D–F, H, I, K, and L). Data are means ± SEM (D–F, H, I, K, and L). Scale bars: 100 μm (low magnification in C), 20 μm (high magnification in C), 200 μm (G), 200 μm (low magnification in J), and 50 μm (high magnification in J).

Please cite this article in press as: Kong et al., Clonally expanded, targetable, natural killer-like NKG7 T cells seed the aged spinal cord to disrupt myeloid-dependent wound healing, Neuron (2024), https://doi.org/10.1016/j.neuron.2024.12.012

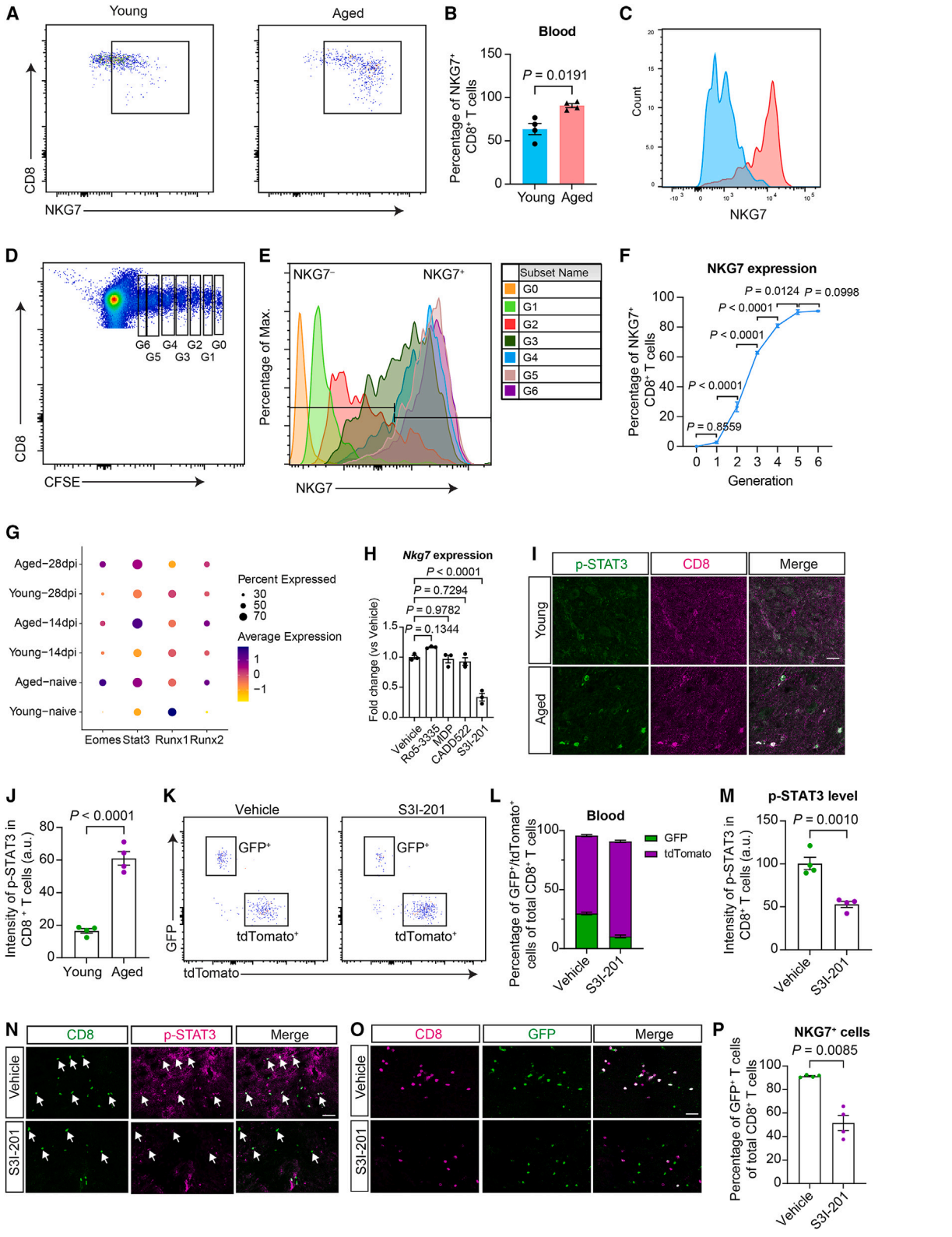

(legend on next page)

Please cite this article in press as: Kong et al., Clonally expanded, targetable, natural killer-like NKG7 T cells seed the aged spinal cord to disrupt myeloid-dependent wound healing, Neuron (2024), https://doi.org/10.1016/j.neuron.2024.12.012

prevented branch retraction in Iba1$^+$ cells and reduced the degree of fibronectin-positive scar tissue and of glial fibrillary acidic protein (GFAP)-positive astrocytic borders, as well as of axonal dieback, after SCI (Figures 7B–7E, 7I–7K, and S18A–S18C). Despite an equal number of CD8$^+$ T cells, *Nkg7* deletion led to retention of GZMK inside CD8$^+$ T cells, in keeping with a role for *Nkg7* in T cell degranulation (Figures 7F–7H). Flow cytometry confirmed the absence of NKG7$^+$CD8$^+$ T cells in the blood, spinal cord, and bone marrow of mice reconstituted with *Nkg7*$^{-/-}$ mouse bone marrow (Figures 7L–7P and S19A–S19C). Deletion of *Nkg7* in CD8$^+$ T cells in the young did not improve fibrosis of the spinal cord after injury (Figures S20A–S20D). Together, these data provide evidence that *Nkg7* deletion in CD8$^+$ T cells promotes repair after SCI and prevents activation of IAM in aged mice.

CD8$^+$ T cell neutralization attenuates the aging-dependent inflammatory myeloid cell phenotype and promotes wound healing and neurological recovery after SCI

To test whether CD8$^+$ T cell neutralization in aged animals would promote wound healing, anti-CD8 monoclonal antibodies or control IgG were delivered i.p. 4 h post SCI in the mouse biweekly until sacrifice 8 weeks post injury. As expected, CD8$^+$ T cell antagonism led to a significant reduction in CD8$^+$ T cells in both the peripheral blood (Figures S21A and S21B) and within the injured spinal cord (Figures S21C and S21D). Strikingly, CD8 neutralization decreased axon retraction and enhanced sparing of sensory and motor axons as well as of serotonergic fibers on lumbar motor neurons (Figures S21E–S21I). Further, scRNA-seq was performed 4 weeks after SCI and CD8$^+$ T cell neutralization to explore whether CD8$^+$ T cell antagonism would affect the glial and immune cells that mediate wound healing. As expected, scRNA-seq analysis showed that the number of CD8$^+$ T cells was reduced (Figures S22A and S22B). Importantly, scRNA-seq also revealed that CD8$^+$ T cell neutralization mainly affected the molecular response of antigen-presenting myeloid cells such as microglia and macrophages. These cells displayed a reduction of interferon-mediated pro-inflammatory function and an induction of type 2 immunity as well as wound repair and angiogenesis responses, suggesting a possible shift toward a wound-healing functional profile (Figures 8A–8E and S22C–S22G; Tables S6, S7, S8, S9, S10, and S11).

Lastly, it was investigated whether functional neurological recovery was achievable in a clinically highly relevant model of severe spinal crush injury in the aged mouse with CD8$^+$ T cell neutralization within the CNS. Anti-CD8 monoclonal antibodies or IgG were delivered via a subcutaneous minipump connected to an intracerebroventricular catheter from the day of surgery until 10 weeks post injury, when sensory and motor corticospinal tracts were traced before mice were sacrificed 2 weeks later (Figure 8F). Indeed, this approach completely depleted CD8$^+$ T cells (Figures S23A–S23D). CD8$^+$ T cell depletion led to a remarkable reduction in GZMK release, preventing the activation of Iba1$^+$ IAM (Figures 8M–8O and S24A). This occurred concomitantly with improved wound healing as shown by an increased vascularization and reduction in the fibrotic scar (Figures S24B–S24F). Treatment also enhanced sparing of serotonergic axons on lumbar motor neurons and attenuated axonal dieback of sensory and motor axons (Figures 8G–8K). Importantly, despite the severity of the injury and the marked neurological impairment in IgG-treated mice, CD8$^+$ T cell depletion significantly ameliorated motor dysfunction as shown by open field locomotion assessment (Basso mouse scale [BMS]) and by measuring the number of missteps on a grid walk (Figures 8P and 8Q). Together, these studies demonstrate that neutralization of CD8$^+$ T cells improves spinal cord wound healing, sensorimotor axonal retraction, sparing of serotonergic axons on lumbar motor neurons, and locomotor recovery.

DISCUSSION

This study reports the novel identification of exhausted and hyperactive NKG7$^+$CD8$^+$ NKLT cells that seed the aged spinal

Figure 6. Expression level of NKG7 correlates with cell activation and requires p-STAT3 in CD8$^+$ T cells

(A and B) Representative flow cytometry plots (A) and quantification (B) of NKG7$^+$CD8$^+$ T cell percentage of total CD8$^+$ T cells from blood (n = 4 biological replicates in each group).

(C) Histogram showing the expression level of NKG7 in CD8$^+$ T cells in the blood of young versus aged mice.

(D) Representative flow cytometry plot shows carboxyfluorescein succinimidyl ester (CFSE)-labeled generations (G0 to G6) of adoptively transferred OT-I *Rag2*$^{-/-}$ CD8$^+$ T cells in the spleen of WT recipients following SIINFEKL stimulation *in vivo*.

(E) Histogram shows expression levels of NKG7 in each generation of OT-I CD8$^+$ T cells in (D).

(F) Quantification of percentage of NKG7$^+$CD8$^+$ T cells of total CD8$^+$ T cells in each generation in (D) (n = 3 biological replicates).

(G) Dot plot shows the expression level of the predicated transcription factors of Nkg7 in different conditions.

(H) *Nkg7* transcription factor screening by qPCR using selective compounds, including Ro5-3335 (RUNX1 inhibitor), MDP (RUNX agonist), CADD522 (RUNX2 inhibitor), and S3I-201 (STAT3 inhibitor), in primary CD8$^+$ T cell culture (n = 3 biological replicates in each group).

(I) Immunostaining of p-STAT3 and CD8 in the spinal cord lesion site in both young and aged mice 14 days post injury (dpi).

(J) Quantification of p-STAT3 in CD8$^+$ T cells of (I) (n = 4 biological replicates in each group).

(K and L) Flow cytometry analysis of GFP$^+$ (NKG7$^+$ cells) versus tdTomato$^+$ (NKG7$^-$ cells) CD8$^+$ T cells in the blood of *Nkg7*-cre × mT/mG mice after the delivery of vehicle or S3I-201.

(M and N) Co-staining of CD8 and p-STAT3 indicates the inhibition of p-STAT3 in CD8$^+$ T cells at the spinal cord lesion site 14 dpi in aged *Nkg7*-cre × mT/mG BMC mice after the delivery of S3I-201 or vehicle (n = 4 biological replicates in each group). Arrowheads indicate the reduced expression of p-STAT3 in CD8$^+$ T cells after S3I-201 or vehicle treatment.

(O and P) Immunostaining and quantification of GFP$^+$ CD8$^+$ T cells in the spinal cord lesion site after the delivery of vehicle or S3I-201 in aged *Nkg7*-cre × mT/mG BMC mice 14 dpi. Double-labeled cells are visible in white.

Unpaired two-tailed t test with Welch's correction (B, J, M, and P). One-way ANOVA followed by post hoc Tukey's test (F). One-way ANOVA followed by post hoc Dunnett's test (H). Data are means ± SEM (B, F, H, J, M, and P). Scale bars: 20 μm (I) and 50 μm (N and O).

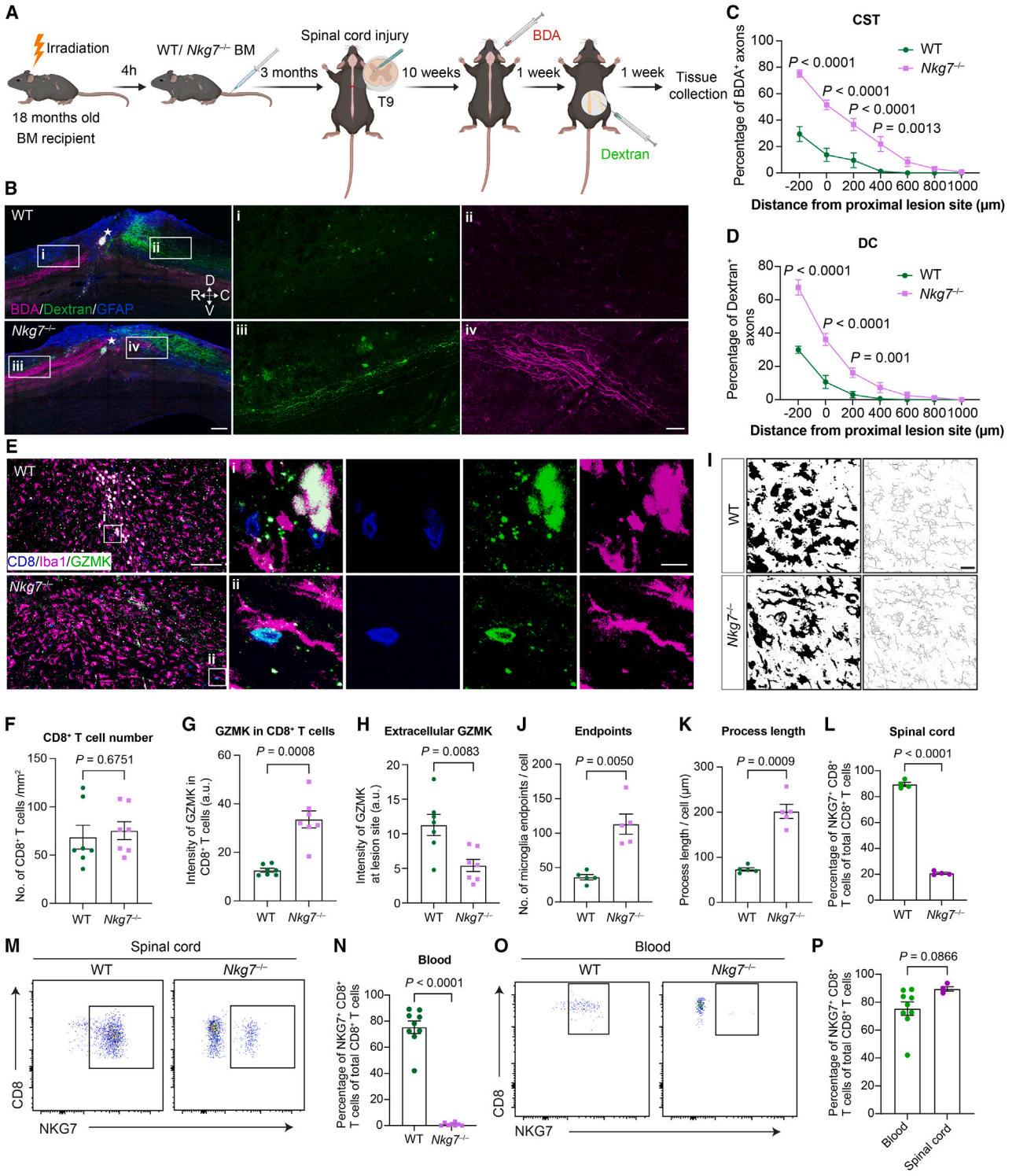

Figure 7. *Nkg7* deletion in CD8⁺ T cells promotes wound healing and axon growth and reduces degranulation of granzyme K after SCI

(A) Experimental workflow of WT/*Nkg7*$^{-/-}$ bone marrow chimera (BMC) followed by SCI and axonal tracing.

(B) Representative images of dorsal column (DC) axons labeled with dextran and descending cortical spinal tracts (CSTs) labeled with biotinylated dextran amine (BDA) co-stained with GFAP on sagittal sections of spinal cord from aged WT or *Nkg7*$^{-/-}$ chimeric mice after SCI. High-magnification images (i and ii) show axons in the spinal cord of *Nkg7*$^{-/-}$ chimeric mice.

(legend continued on next page)

Please cite this article in press as: Kong et al., Clonally expanded, targetable, natural killer-like NKG7 T cells seed the aged spinal cord to disrupt myeloid-dependent wound healing, Neuron (2024), https://doi.org/10.1016/j.neuron.2024.12.012

cord and clonally expand after engaging with myeloid cells. NKLT cells are found in both humans and mice. NKLT cells express high levels of GZMK that are found highly expressed within myeloid cells. However, NKG7 deletion reduces the amount of GZMK found in the extracellular space and within myeloid cells, increasing its expression within NKLT cells, suggesting retention due to impaired degranulation. The spinal cord tissue residency of NKG7$^+$CD8$^+$ NKLT cells prior to an injury in aged mice causes a loss of the expected temporal coordination of innate immunity preceding adoptive T cell responses after injury, which likely limits wound healing. Importantly, NKG7 deletion attenuated tissue damage, as shown by using a mouse chimera where CD8$^+$ T cells lack *Nkg7*, and the clinically suitable neutralization of CD8$^+$ T cells in the cerebrospinal fluid (CSF) with monoclonal antibodies after SCI promoted repair and recovery.

Nkg7 deletion or CD8$^+$ T cell antagonism promotes wound healing by reducing the fibrotic scar and axon retraction as well as by promoting vascularization and axon sparing. Remarkably, depletion of CD8$^+$ T cells promotes neurological recovery in a model of severe spinal cord crush injury in aged mice, where disability is otherwise permanent and severe.

The NK-like features of NKG7$^+$CD8$^+$ T cells are in line with their cytotoxic activity that is initiated shortly after an injury. However, their peculiarity is their prominent clonal expansion and hyperactivation in the aged mouse and following SCI. This phenotype is unlike that of senescent NKT and T cells that typically degranulate in an antigen non-specific manner and have poor clonal expansion ability.[25]

Interestingly, while the spinal cord NKG7$^+$CD8$^+$ NKLT cells identified are detrimental to repair, the role of senescent T cells remains controversial, exerting both protective and cytotoxic effects.[25,26] Yet, our study found that NKG7$^+$CD8$^+$ exhausted NKLT cells also displayed prominent clonal expansion, signs of hyperactivity, and tissue retention and were localized to the spinal cord 12 weeks after injury in aged mice. Notably, NKLT cells in the aged and post-injury spinal cord do not display markers of tissue residence, tissue memory, or regulatory profiles.

While NKG7$^+$ T cells have been described to have a role in antitumor immunity,[27] in the protective immune response against visceral leishmaniasis and malaria,[24] their role in the CNS has thus far remained elusive. Our findings indicate that the CD8$^+$ T cells expressing the granule proteins NKG7 and GZMK not only defend against cancer and infection but are cytotoxic after SCI by targeting macrophage/microglia cells, thus enhancing tissue damage. This claim is underscored by the reversal of the phenotype in mouse chimera experiments with CD8$^+$ T cells lacking NKG7. Importantly, NKG7 expression in CD8$^+$ T cells was found in the human injured spinal cord, suggesting relevance to human disease in both middle-aged and aged individuals.

Unfortunately, spinal cord tissue from young injured individuals could not be obtained to compare the abundance of CD8$^+$ T cells with middle-aged and elderly subjects.

How NKG7 precisely exerts cytotoxicity remains undetermined; however, our data suggest a key role in degranulation. Cytotoxic CD8$^+$ T cells were found in proximity to IAM, where they degranulate as shown by GZMK expression. Our data indicate that this process impairs the wound-healing ability of MHC-I-expressing IAM. Interestingly, these myeloid cells express elevated levels of *Cxcl16*, which is needed to allow the accumulation of CXCR6-expressing cytotoxic CD8$^+$ T cells in the spinal cord, suggestive of a pathogenic loop mechanism. Both morphological studies and scRNA-seq experiments after CD8$^+$ T cell depletion and SCI highlight a prominent role for CD8$^+$ T cells in regulating the phenotypes of innate immune cells. These innate immune cells show an enhanced inflammatory profile and reduced wound-healing properties in the aged injured spinal cord that are reversed by CD8$^+$ T cell depletion. The myeloid cell wound-healing phenotype in proximity to the injury is also normalized in the NKG7 null mouse chimera that show retention of GZMK. Together, these data suggest that NKG7$^+$ NKLT cells impair innate immune-dependent wound healing.

Intriguingly, this mechanism is unlike our previous observation in the peripheral nervous system after sciatic nerve injury, where a distinct population of CD8$^+$ T cells without NKLT signatures was found far away from the injury site. In that instance, classical CD8$^+$ T cells engaged directly with MHC-I in sensory neurons to restrict axonal regeneration[28] and played no role in tissue damage or wound healing.

Studies in brain and spinal cord animal models of neurodegeneration or injury, as well as in CSF of aged individuals, have found a variety of T cell subtypes, including tissue memory, effector memory, regulatory, and cytotoxic T cells with varying neuroprotective or cytotoxic properties.[29–33] Additionally, while each study described the prevalence of one T cell subtype, they also recognized diverse T cell populations. By contrast, our study identified a rather homogeneous population of clonally expanded cytotoxic T cells already residing in the spinal cord of aged mice preceding an injury. This suggests remarkably

(C and D) Quantification of caudal DC (C) (n = 6 and 5 biological replicates for WT and *Nkg7*$^{-/-}$ groups, respectively) and rostral CST (D) (n = 4 and 4 biological replicates for WT and *Nkg7*$^{-/-}$ groups) axon labeling.
(E) Representative images of immunostained lesion site of sagittal spinal cord sections with the antibodies against CD8, Iba1, and GZMK in aged WT versus *Nkg7*$^{-/-}$ chimeric mice.
(F–H) Quantification of the number of CD8$^+$ T cells (F), expression of GZMK in CD8$^+$ T cells (G), and outside of CD8$^+$ T cells (H) (n = 7 in each group).
(I) Skeleton images show the ramification of Iba1$^+$ cells in WT and *Nkg7*$^{-/-}$ BMC mice.
(J and K) Quantification of endpoints number (J) and process length (K) of Iba1$^+$ cells in (I) (n = 5 biological replicates in each group).
(L and M) Representative flow cytometry plots (M) and quantification (L) of the expression of NKG7 in CD8$^+$ T cells in the spinal cord of aged WT versus *Nkg7*$^{-/-}$ BMC mice 3 months after irradiation and bone marrow (BM) transplantation. (n = 4 in each group.)
(N and O) Representative flow cytometry plots (O) and quantification (N) of the expression of NKG7 in CD8$^+$ T cells in the blood of aged WT versus *Nkg7*$^{-/-}$ BM chimeric mice 3 months after irradiation and BM transplantation. (n = 9 and 8 biological replicates for WT and *Nkg7*$^{-/-}$ BM chimeric mice, respectively.)
(P) Quantification of NKG7$^+$ CD8$^+$ T cells in the spinal cord of the WT chimeras paired with the blood-derived cells (n = 4 biological replicates in each group).
Two-way ANOVA followed by post hoc Sidak's test (C and D). Unpaired two-sided t test with Welch's correction (F–H, J, K, N, and P). Data are means ± SEM (C, D, F–H, J–L, N, and P). Scale bars: 100 μm (low magnification in B and E), 20 μm (high magnification in B), 10 μm (high magnification in E), 50 μm (I).

Please cite this article in press as: Kong et al., Clonally expanded, targetable, natural killer-like NKG7 T cells seed the aged spinal cord to disrupt myeloid-dependent wound healing, Neuron (2024), https://doi.org/10.1016/j.neuron.2024.12.012

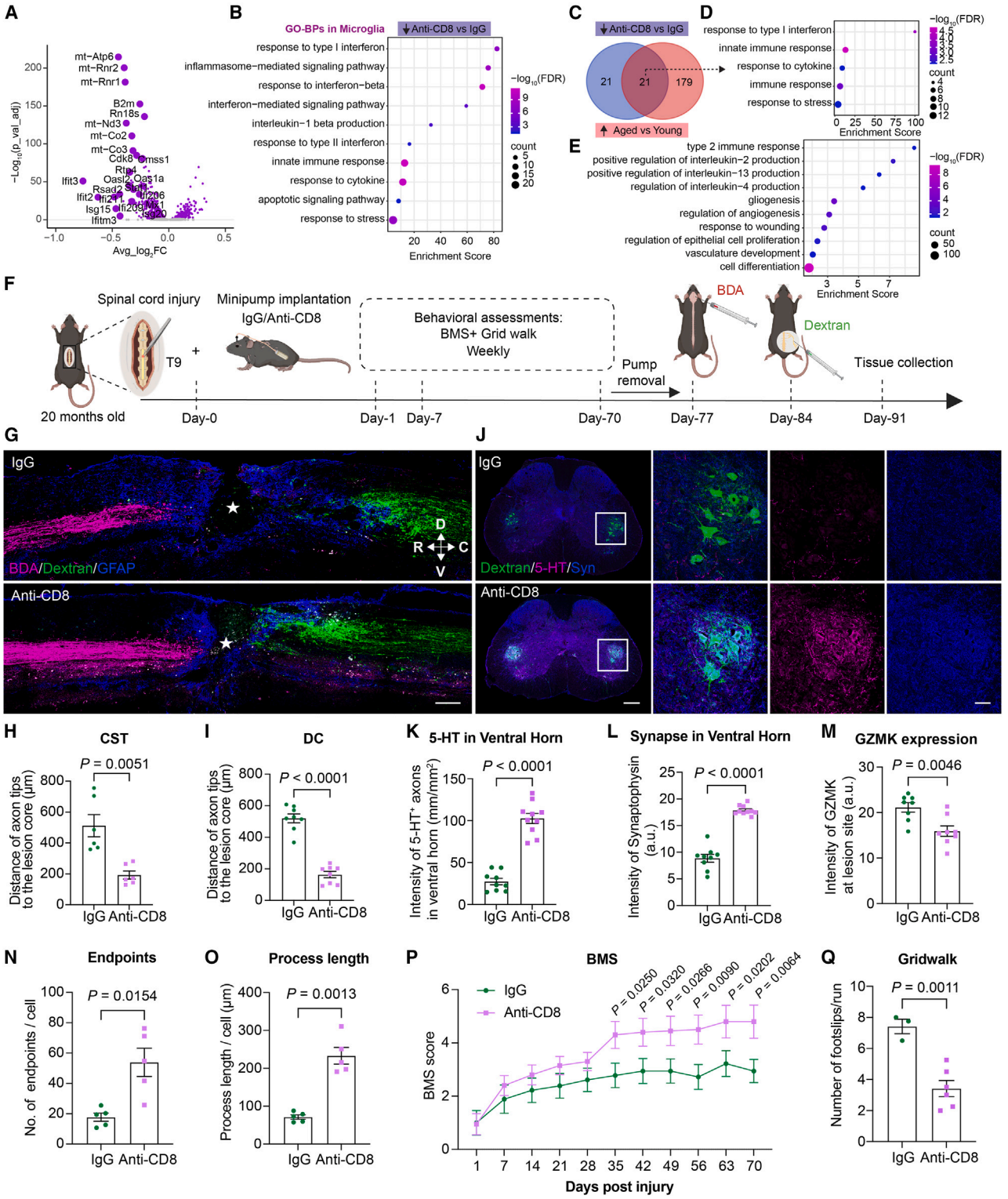

Figure 8. Neutralization of CD8⁺ T cells facilitates wound healing and functional recovery after SCI

(A) Volcano plot shows the DE genes of anti-CD8 versus IgG in microglia.

(B) Gene Ontology-Biological Processes (GO-BPs) analysis using significantly downregulated genes (adjusted $p < 0.05$, $\log_2$fold change < -0.25) in microglia after CD8⁺ T cell depletion showing reduced interferon-mediated pro-inflammatory responses.

(C) Venn diagram showing 21 common significantly DE genes in microglia upregulated by aging and reversed by depletion of CD8⁺ T cells after SCI.

(legend continued on next page)

unique properties of the aged spinal cord versus the brain, whose mechanistic explanation remains elusive.

Altogether, it seems unlikely that general rules governing whether $CD8^+$ T cells are neuroprotective or cytotoxic in the injured nervous system might be leveraged for treatment.[34] The specific molecular subset, the similarity to NK or NKT cells, the localization to the brain or spinal cord, the age, the specific type of injury, and the post-injury acute versus chronic state are likely all essential variables to consider.

Since adaptive immunity has been increasingly targeted with monoclonal antibodies,[35] our evidence in the mouse and human injured spinal cord for cytotoxic $CD8^+$ T cells seems to have a realistic clinical translational potential.

Most studies in experimental SCI include young animals with a more favorable repair ability that poorly represent clinical SCI across the lifespan of an adult individual. However, it has been recently found that systemic depletion of $CD8^+$ T cells in the aged spinal cord after injury reduced the differentiation of NSCs into astrocytes and promoted the differentiation of NSCs into oligodendrocytes as well as functional recovery.[36] While systemic depletion of $CD8^+$ T cells presents the risk of immunosuppression, our findings suggest that targeting $CD8^+$ T cells in the CNS with monoclonal antibodies in the cerebrospinal fluid with osmotic minipumps implanted at the time of spinal cord decompressive surgery could represent a novel therapeutic option with likely lesser risk for systemic immunosuppression. In fact, this strategy has the potential to enhance wound healing and axonal sparing, as well as promote neurological recovery when repair is especially challenging, as in clinical SCI.

RESOURCE AVAILABILITY

Lead contact

Requests for further information and for resources and reagents should be directed to and will be fulfilled by the lead contact, Simone Di Giovanni (s.di-giovanni@imperial.ac.uk).

Materials availability

This study did not generate new, unique reagents.

Data and code availability

- scRNA-seq and scTCR-seq data have been deposited at GEO and are publicly available as of the date of publication. The accession numbers are listed in the key resources table.
- This paper does not report original code.
- Any additional information required to reanalyze the data reported in this paper is available from the lead contact upon request.

ACKNOWLEDGMENTS

This work was supported by the United States Department of Defense (S.D.G.), the Guarantors of Brain (L.Z.), the Marina Romoli Foundation (S.D.G.), Wings for Life (S.D.G.), The Rosetrees Trust (S.D.G.), The Adelson Medical Research Foundation (S.D.G.), and the UK Medical Research Council (S.D.G., MRC grant MR/M501797/1). The research was supported by the National Institute for Health Research (NIHR) Imperial Biomedical Research Centre (S.D.G.). The views expressed are those of the author(s) and not necessarily those of the NHS, the NIHR, or the Department of Health. We also would like to thank Drs. Ann McKee, Thor Stein, and Bertrand Huber for autopsy and diagnosis of human spinal cord samples and assistance in optimizing human T cell antibodies.

AUTHOR CONTRIBUTIONS

G.K. and L.Z. designed and performed experiments, analyzed data, and wrote the manuscript. Y.S. and Y.Y. performed behavioral experiments. S.M.C. performed immunostaining of the naive human spinal experiment and data analysis. M.S.S. performed data analysis. F.D.L.R. performed a WT and *Nkg7*$^{-/-}$ bone marrow cell extraction experiment. J.D.C., E.A.A., V.S., R.K., B.K.K., and C.R.E. provided experimental advice and edited the manuscript. N.E. performed experiments. A.V. provided the injured human spinal cord sections. S.S.N. provided experimental advice. S.D.G. designed experiments, provided funding, and wrote the manuscript.

DECLARATION OF INTERESTS

The authors declare no competing interests.

STAR★METHODS

Detailed methods are provided in the online version of this paper and include the following:

- KEY RESOURCES TABLE
- EXPERIMENTAL MODEL AND STUDY PARTICIPANT DETAILS
  - Mice
  - Human material
- METHOD DETAILS
  - Spinal cord injury
  - Axonal tracing
  - Tissue dissociation
  - Cell sorting

(D) GO-BPs analysis of common genes in (C) showing aging-induced pro-inflammatory pathways in microglia counteracted by depletion of $CD8^+$ T cells.
(E) Significantly induced genes ($p < 0.05$, $\log_2$fold change > 0.25) in macrophage cluster 4 enriched in anti-inflammation-associated signaling pathways and wound-healing processes.
(F) Experimental procedure of osmotic minipump implantation and intracerebroventricular (ICV) antibody delivery followed by sensorimotor functional assessments and SCI.
(G) Representative images of spinal cord sagittal sections showing dextran-labeled DC axons (green) and CST (magenta). Asterisks showing the lesion core.
(H and I) Quantification of the distance of CST (H) or DC (I) axon tips from the lesion core ($n = 6$ and 8 biological replicates for CST and DC groups, respectively).
(J) Representative images of 5-hydroxytryptamine (5-HT)-positive axons around the motor neurons labeled with dextran co-stained with synaptophysin (Syn) in the lumbar ventral horn.
(K and L) Quantification of the intensity of 5-HT axons (K) and synaptophysin (L) in the ventral horn of lumbar spinal cord ($n = 9$ and 10 biological replicates for IgG and anti-CD8 groups, respectively).
(M) Quantification of GZMK expression at the lesion site ($n = 8$ biological replicates).
(N and O) Quantification of endpoint number (N) and process length (O) of $Iba1^+$ myeloid cells ($n = 5$ biological replicates).
(P and Q) Quantification of BMS sore ($n = 9$ and 10 biological replicates for IgG control and $CD8^+$ T cell depletion groups, respectively) (P) and number of foot slips in grid walk test (Q) ($n = 3/9$ and 6/10 biological replicates for IgG and anti-CD8 antibody-delivered mice with BMS sore ≥ 4, respectively).
Wilcox rank-sum tests (A). Unpaired two-tailed t test with Welch's correction (H, I, K–O, and Q). Two-way ANOVA followed by post hoc Sidak's test (P). Data are means ± SEM (H, I, and K–Q). Scale bars: 200 μm (G and low magnification in J) and 50 μm (high magnification in J).

SUPPLEMENTAL INFORMATION

Supplemental information can be found online at https://doi.org/10.1016/j.neuron.2024.12.012.

Received: March 19, 2024
Revised: October 7, 2024
Accepted: December 12, 2024
Published: January 13, 2025

REFERENCES

1. GBD Spinal Cord Injuries Collaborators (2023). Global, regional, and national burden of spinal cord injury, 1990–2019: a systematic analysis for the Global Burden of Disease Study 2019. Lancet Neurol. *22*, 1026–1047. https://doi.org/10.1016/S1474-4422(23)00287-9.
2. Lu, Y., Shang, Z., Zhang, W., Pang, M., Hu, X., Dai, Y., Shen, R., Wu, Y., Liu, C., Luo, T., et al. (2024). Global incidence and characteristics of spinal cord injury since 2000–2021: a systematic review and meta-analysis. BMC Med. *22*, 285. https://doi.org/10.1186/s12916-024-03514-9.
3. Liu, Y., Yang, X., He, Z., Li, J., Li, Y., Wu, Y., Manyande, A., Feng, M., and Xiang, H. (2023). Spinal cord injury: global burden from 1990 to 2019 and projections up to 2030 using Bayesian age-period-cohort analysis. Front. Neurol. *14*, 1304153. https://doi.org/10.3389/fneur.2023.1304153.
4. Eisenberg, M.G., and Saltz, C.C. (1991). Quality of life among aging spinal cord injured persons: long term rehabilitation outcomes. Paraplegia *29*, 514–520.
5. Geoffroy, C.G., Hilton, B.J., Tetzlaff, W., and Zheng, B. (2016). Evidence for an age-dependent decline in axon regeneration in the adult mammalian central nervous system. Cell Rep. *15*, 238–246.
6. Furlan, J.C. (2022). Effects of age on survival and neurological recovery of individuals following acute traumatic spinal cord injury. Spinal Cord *60*, 81–89. https://doi.org/10.1038/s41393-021-00719-0.
7. Furlan, J.C., and Fehlings, M.G. (2009). The impact of age on mortality, impairment, and disability among adults with acute traumatic spinal cord injury. J. Neurotrauma *26*, 1707–1717. https://doi.org/10.1089/neu.2009.0888.
8. Ding, W., Hu, S., Wang, P., Kang, H., Peng, R., Dong, Y., and Li, F. (2022). Spinal Cord Injury: The Global Incidence, Prevalence, and Disability From the Global Burden of Disease Study 2019. Spine *47*, 1532–1540. https://doi.org/10.1097/BRS.0000000000004417.
9. Brennan, F.H., Li, Y., Wang, C., Ma, A., Guo, Q., Li, Y., Pukos, N., Campbell, W.A., Witcher, K.G., Guan, Z., et al. (2022). Microglia coordinate cellular interactions during spinal cord repair in mice. Nat. Commun. *13*, 4096.
10. Milich, L.M., Choi, J.S., Ryan, C., Cerqueira, S.R., Benavides, S., Yahn, S.L., Tsoulfas, P., and Lee, J.K. (2021). Single-cell analysis of the cellular heterogeneity and interactions in the injured mouse spinal cord. J. Exp. Med. *218*, e20210040.
11. Zha, J., Smith, A., Andreansky, S., Bracchi-Ricard, V., and Bethea, J.R. (2014). Chronic thoracic spinal cord injury impairs CD8+ T-cell function by up-regulating programmed cell death-1 expression. J. Neuroinflammation *11*, 65. https://doi.org/10.1186/1742-2094-11-65.
12. Jones, T.B., Hart, R.P., and Popovich, P.G. (2005). Molecular control of physiological and pathological T-cell recruitment after mouse spinal cord injury. J. Neurosci. *25*, 6576–6583. https://doi.org/10.1523/JNEUROSCI.0305-05.2005.
13. Jogia, T., Kopp, M.A., Schwab, J.M., and Ruitenberg, M.J. (2021). Peripheral white blood cell responses as emerging biomarkers for patient stratification and prognosis in acute spinal cord injury. Curr. Opin. Neurol. *34*, 796–803. https://doi.org/10.1097/WCO.0000000000000995.
14. Raposo, C., Graubardt, N., Cohen, M., Eitan, C., London, A., Berkutzki, T., and Schwartz, M. (2014). CNS repair requires both effector and regulatory T cells with distinct temporal and spatial profiles. J. Neurosci. *34*, 10141–10155. https://doi.org/10.1523/JNEUROSCI.0076-14.2014.
15. Shechter, R., London, A., and Schwartz, M. (2013). Orchestrated leukocyte recruitment to immune-privileged sites: absolute barriers versus educational gates. Nat. Rev. Immunol. *13*, 206–218. https://doi.org/10.1038/nri3391.
16. Hauben, E., Butovsky, O., Nevo, U., Yoles, E., Moalem, G., Agranov, E., Mor, F., Leibowitz-Amit, R., Pevsner, E., Akselrod, S., et al. (2000). Passive or active immunization with myelin basic protein promotes recovery from spinal cord contusion. J. Neurosci. *20*, 6421–6430. https://doi.org/10.1523/JNEUROSCI.20-17-06421.2000.
17. Gadani, S.P., Smirnov, I., Wiltbank, A.T., Overall, C.C., and Kipnis, J. (2017). Characterization of meningeal type 2 innate lymphocytes and their response to CNS injury. J. Exp. Med. *214*, 285–296. https://doi.org/10.1084/jem.20161982.
18. Siegenthaler, M.M., Ammon, D.L., and Keirstead, H.S. (2008). Myelin pathogenesis and functional deficits following SCI are age-associated. Exp. Neurol. *213*, 363–371. https://doi.org/10.1016/j.expneurol.2008.06.015.
19. Salvador, A.F.M., Dykstra, T., Rustenhoven, J., Gao, W., Blackburn, S.M., Bhasiin, K., Dong, M.Q., Guimarães, R.M., Gonuguntla, S., Smirnov, I., et al. (2023). Age-dependent immune and lymphatic responses after spinal cord injury. Neuron *111*, 2155–2169.e9. https://doi.org/10.1016/j.neuron.2023.04.011.
20. Takano, M., Kawabata, S., Shibata, S., Yasuda, A., Nori, S., Tsuji, O., Nagoshi, N., Iwanami, A., Ebise, H., Horiuchi, K., et al. (2017). Enhanced functional recovery from spinal cord injury in aged mice after stem cell transplantation through HGF induction. Stem Cell Rep. *8*, 509–518. https://doi.org/10.1016/j.stemcr.2017.01.013.
21. Norton, W.T., Aquino, D.A., Hozumi, I., Chiu, F.C., and Brosnan, C.F. (1992). Quantitative aspects of reactive gliosis: a review. Neurochem. Res. *17*, 877–885. https://doi.org/10.1007/BF00993263.
22. Soderblom, C., Luo, X., Blumenthal, E., Bray, E., Lyapichev, K., Ramos, J., Krishnan, V., Lai-Hsu, C., Park, K.K., Tsoulfas, P., and Lee, J.K. (2013). Perivascular fibroblasts form the fibrotic scar after contusive spinal cord injury. J. Neurosci. *33*, 13882–13887. https://doi.org/10.1523/JNEUROSCI.2524-13.2013.
23. Herrmann, J.E., Imura, T., Song, B., Qi, J., Ao, Y., Nguyen, T.K., Korsak, R.A., Takeda, K., Akira, S., and Sofroniew, M.V. (2008). STAT3 is a critical regulator of astrogliosis and scar formation after spinal cord injury. J. Neurosci. *28*, 7231–7243. https://doi.org/10.1523/JNEUROSCI.1709-08.2008.
24. Ng, S.S., De Labastida Rivera, F., Yan, J., Corvino, D., Das, I., Zhang, P., Kuns, R., Chauhan, S.B., Hou, J., Li, X.Y., et al. (2020). The NK cell granule protein NKG7 regulates cytotoxic granule exocytosis and inflammation. Nat. Immunol. *21*, 1205–1218. https://doi.org/10.1038/s41590-020-0758-6.

25. Laphanuwat, P., Gomes, D.C.O., and Akbar, A.N. (2023). Senescent T cells: beneficial and detrimental roles. Immunol. Rev. *316*, 160–175. https://doi.org/10.1111/imr.13206.

26. Wu, Y., Lin, Y.H., Shi, L.L., Yao, Z.F., Xie, X.M., Jiang, Z.S., Tang, J., Hu, J.G., and Lü, H.Z. (2017). Temporal kinetics of $CD8^+$ $CD28^+$ and $CD8^+$ $CD28^-$ T lymphocytes in the injured rat spinal cord. J. Neurosci. Res. *95*, 1666–1676. https://doi.org/10.1002/jnr.23993.

27. Li, X.Y., Corvino, D., Nowlan, B., Aguilera, A.R., Ng, S.S., Braun, M., Cillo, A.R., Bald, T., Smyth, M.J., and Engwerda, C.R. (2022). NKG7 is required for optimal antitumor T-cell immunity. Cancer Immunol. Res. *10*, 154–161. https://doi.org/10.1158/2326-6066.CIR-20-0649.

28. Zhou, L., Kong, G., Palmisano, I., Cencioni, M.T., Danzi, M., De Virgiliis, F., Chadwick, J.S., Crawford, G., Yu, Z., De Winter, F., et al. (2022). Reversible CD8 T cell-neuron cross-talk causes aging-dependent neuronal regenerative decline. Science *376*, eabd5926. https://doi.org/10.1126/science.abd5926.

29. Piehl, N., van Olst, L., Ramakrishnan, A., Teregulova, V., Simonton, B., Zhang, Z., Tapp, E., Channappa, D., Oh, H., Losada, P.M., et al. (2022). Cerebrospinal fluid immune dysregulation during healthy brain aging and cognitive impairment. Cell *185*, 5028–5039.e13. https://doi.org/10.1016/j.cell.2022.11.019.

30. Altendorfer, B., Unger, M.S., Poupardin, R., Hoog, A., Asslaber, D., Gratz, I.K., Mrowetz, H., Benedetti, A., de Sousa, D.M.B., Greil, R., et al. (2022). Transcriptomic Profiling Identifies $CD8^+$ T Cells in the Brain of Aged and Alzheimer's Disease Transgenic Mice as Tissue-Resident Memory T Cells. J. Immunol. *209*, 1272–1285. https://doi.org/10.4049/jimmunol.2100737.

31. Chen, X., Firulyova, M., Manis, M., Herz, J., Smirnov, I., Aladyeva, E., Wang, C., Bao, X., Finn, M.B., Hu, H., et al. (2023). Microglia-mediated T cell infiltration drives neurodegeneration in tauopathy. Nature *615*, 668–677. https://doi.org/10.1038/s41586-023-05788-0.

32. Jafarzadeh, A., Sheikhi, A., Jafarzadeh, Z., and Nemati, M. (2023). Differential roles of regulatory T cells in Alzheimer's disease. Cell. Immunol. *393–394*, 104778. https://doi.org/10.1016/j.cellimm.2023.104778.

33. Su, W., Saravia, J., Risch, I., Rankin, S., Guy, C., Chapman, N.M., Shi, H., Sun, Y., Kc, A., Li, W., et al. (2023). CXCR6 orchestrates brain $CD8^+$T cell residency and limits mouse Alzheimer's disease pathology. Nat. Immunol. *24*, 1735–1747. https://doi.org/10.1038/s41590-023-01604-z.

34. Hu, D., Xia, W., and Weiner, H.L. (2022). $CD8^+$ T cells in neurodegeneration: friend or foe? Mol. Neurodegener. *17*, 59. https://doi.org/10.1186/s13024-022-00563-7.

35. Alejandra, W.P., Miriam Irene, J.P., Fabio Antonio, G.S., Patricia, R.R., Elizabeth, T.A., Aleman-Aguilar, J.P., and Rebeca, G.V. (2023). Production of monoclonal antibodies for therapeutic purposes: A review. Int. Immunopharmacol. *120*, 110376. https://doi.org/10.1016/j.intimp.2023.110376.

36. Wang, J., Xu, L., Peng, D., Zhu, Y., Gu, Z., Yao, Y., Li, H., Cao, X., Fu, C.Y., Zheng, M., et al. (2023). IFN-γ-STAT1-mediated $CD8^+$ T-cell-neural stem cell cross talk controls astrogliogenesis after spinal cord injury. Inflamm. Regen. *43*, 12. https://doi.org/10.1186/s41232-023-00263-9.

37. Butler, A., Hoffman, P., Smibert, P., Paplexi, E., and Satija, R. (2018). Integrating single-cell transcriptomic data across different conditions, technologies, and species. Nat. Biotechnol. *36*, 411–420. https://doi.org/10.1038/nbt.4096.

38. McGinnis, C.S., Murrow, L.M., and Gartner, Z.J. (2019). DoubletFinder: Doublet Detection in Single-Cell RNA Sequencing Data Using Artificial Nearest Neighbors. Cell Syst. *13*, 329–337.e4. https://doi.org/10.1016/j.cels.2019.03.003.

39. Jin, S., Guerrero-Juarez, C.F., Zhang, L., Chang, I., Ramos, R., Kuan, C.-H., Myung, P., Plikus, M.V., and Nie, Q. (2021). Inference and analysis of cell-cell communication using CellChat. Nat. Communi. *12*, 1088. https://doi.org/10.1038/s41467-021-21246-9.

40. Kolmykov, S., Yevshin, I., Kulyashov, M., Sharipov, R., Kondrakhin, Y., Makeev, V.J., Kulakovskiy, I.V., Kel, A., and Kolpakov, F. (2021). GTRD: an integrated view of transcription regulation. Nucleic Acids Res. *49*, D104–D111. https://doi.org/10.1093/nar/gkaa1057.

41. Müller, F., De Virgiliis, F., Kong, G., Zhou, L., Serger, E., Chadwick, J., Sanchez-Vassopoulos, A., Singh, A.K., Eswaramoorthy, M., Kundu, T.K., and Di Giovanni, S. (2022). CBP/p300 activation promotes axon growth, sprouting, and synaptic plasticity in chronic experimental spinal cord injury with severe disability. PLoS Biol. *20*, e3001310. https://doi.org/10.1371/journal.pbio.3001310.

42. Hutson, T.H., Kathe, C., Palmisano, I., Bartholdi, K., Hervera, A., De Virgiliis, F., McLachlan, E., Zhou, L., Kong, G., Barraud, Q., et al. (2019). Cbp-dependent histone acetylation mediates axon regeneration induced by environmental enrichment in rodent spinal cord injury models. Sci. Transl. Med. *11*, eaaw2064. https://doi.org/10.1126/scitranslmed.aaw2064.

43. De Virgiliis, F., Hutson, T.H., Palmisano, I., Amachree, S., Miao, J., Zhou, L.M., Todorova, R., Thompson, R., Danzi, M.C., Lemmon, V.P., et al. (2020). Enriched conditioning expands the regenerative ability of sensory neurons after spinal cord injury via neuronal intrinsic redox signaling. Nat. Commun. *11*, 6425. https://doi.org/10.1038/s41467-020-20179-z.

44. Vidal-Itriago, A., Radford, R.A.W., Aramideh, J.A., Maurel, C., Scherer, N.M., Don, E.K., Lee, A., Chung, R.S., Graeber, M.B., and Morsch, M. (2022). Microglia morphophysiological diversity and its implications for the CNS. Front. Immunol. *13*, 997786. https://doi.org/10.3389/fimmu.2022.997786.

Please cite this article in press as: Kong et al., Clonally expanded, targetable, natural killer-like NKG7 T cells seed the aged spinal cord to disrupt myeloid-dependent wound healing, Neuron (2024), https://doi.org/10.1016/j.neuron.2024.12.012

STAR★METHODS

KEY RESOURCES TABLE

REAGENT or RESOURCE	SOURCE	IDENTIFIER
Antibodies		
TruStain FcX PLUS anti-mouse CD16/32 Antibody (S17011E)	Biolegend	Cat# 156604; RRID: AB_2783138
APC anti-mouse CD45 Antibody (30-F11)	Biolegend	Cat# 103111; RRID: AB_312976
Brilliant Violet 711™ anti-mouse CD8a Antibody (53-6.7)	Biolegend	Cat# 100759; RRID: AB_2563510
Brilliant Violet 605™ anti-mouse CD4 Antibody (RM4-5)	Biolegend	Cat# 100547; RRID: AB_11125962
FITC anti-mouse TCR β chain Antibody (H57-597)	Biolegend	Cat# 109205; RRID: AB_313428
PE/Cyanine5 anti-mouse CD45 Antibody (30-F11)	Biolegend	Cat# 103110; RRID: AB_312975
Brilliant Violet 605™ anti-mouse TCR β chain Antibody (H57-597)	Biolegend	Cat# 109241; RRID: AB_2629563
Brilliant Violet 785™ anti-mouse/human CD11b Antibody (M1/70)	Biolegend	Cat# 101243; RRID: AB_2561373
APC/Fire™ 750 anti-mouse CD4 Antibody (RM4-5)	Biolegend	Cat# 100568; RRID: AB_2629699
FITC anti-mouse CD186 (CXCR6) Antibody (SA051D1)	Biolegend	Cat# 151107; RRID: AB_2572144
APC/Cyanine7 anti-mouse CD69 Antibody (H1.2F3)	Biolegend	Cat# 104525; RRID: AB_10683447
PE anti-TIA-1(NKG7) Antibody (2G9A10F5)	Beckman Coulter	Cat# IM3293; RRID: AB_131247
FITC anti-mouse TCR γ/δ Antibody (GL3)	Biolegend	Cat# 118105; RRID: AB_313829
PE/Cyanine7 anti-mouse NK-1.1 Antibody (S17016D)	Biolegend	Cat# 156513; RRID: AB_2888852
InVivoMAb anti-mouse CD8α (YTS 169.4)	BioXcell	Cat# BE0117; RRID: AB_10950145
InVivoMAb rat IgG2b isotype control (LTF-2)	BioXcell	Cat# BE0090; RRID: AB_1107780
Rat Anti-Mouse Cxcl16 Monoclonal Antibody (142417)	Bio-techne	Cat# MAB503; RRID: AB_2276752
InVivoMAb rat IgG2a isotype control (2A3)	BioXcell	Cat# BE0089; RRID: AB_1107769
Chicken Anti-GFAP Antibody	Abcam	Cat# ab4674; RRID: AB_304558
Rat Anti-Mouse CD31 Antibody(MEC 13.3)	BD Biosciences	Cat# 550274; RRID: AB_393571
Recombinant Rabbit Anti-CD8 alpha Antibody [EPR21769]	Abcam	Cat# ab217344; RRID: AB_2890649
Recombinant Rat Anti-Iba1 Antibody [EPR16589]	Abcam	Cat# ab283346; RRID: AB_3065282
Mouse Anti-Granzyme K Monoclonal Antibody	Proteintech	Cat# 67272-1-Ig; RRID: AB_2882541
Rat Anti-MHC Class I Antibody (ER-HR52)	Novus	Cat# NB100-64952; RRID: AB_964497
Rabbit Anti-Collagen I Antibody	Abcam	Cat# ab21286; RRID: AB_446161
Rabbit Anti-CD3 Antibody [SP7]	Abcam	Cat# ab16669; RRID: AB_443425
Rabbit Anti-Fibronectin Antibody	Millipore	Cat# AB2033; RRID: AB_2105702
Recombinant Rabbit Anti-Iba1 Antibody [EPR16588]	Abcam	Cat# ab178846; RRID: AB_2636859
Chicken Anti-GFAP Antibody	Novus	Cat# NBP1-05198; RRID: AB_1556315

(*Continued on next page*)

Please cite this article in press as: Kong et al., Clonally expanded, targetable, natural killer-like NKG7 T cells seed the aged spinal cord to disrupt myeloid-dependent wound healing, Neuron (2024), https://doi.org/10.1016/j.neuron.2024.12.012

Continued

REAGENT or RESOURCE	SOURCE	IDENTIFIER
Recombinant Rabbit Anti-CD8 alpha Antibody [CAL66]	Abcam	Cat# ab237709; RRID: AB_2892677
Rabbit anti-phospho-Stat3 (Tyr705) (D3A7)	Cell Signaling Technology	Cat# #9145; RRID: AB_2491009
Stat3 (124H6) Mouse mAb	Cell Signaling Technology	Cat# #9139; RRID: AB_331757
GAPDH (14C10) Rabbit mAb	Cell Signaling Technology	Cat# #2118; RRID: AB_561053
Mouse Anti-NKG7 antibody [2G9A10F5]	GeneTex	Cat# GTX01839
Biological samples		
Paraffin embedded naive human spinal cord tissue sections	The UNITE Brain Bank, Boston, United States	N/A
Paraffin embedded injured human spinal cord tissue sections	The International Spinal Cord Injury Biobank (ISCIB), University of British Columbia, Canada	N/A
Chemicals, peptides, and recombinant proteins		
Dextran, Tetramethylrhodamine and biotin, 10,000 MW, Lysine Fixable (mini-Ruby)	Thermo Fisher Scientific	Cat# D3312
Dextran, Alexa Fluor™ 488; 10,000 MW, Anionic, Fixable	Thermo Fisher Scientific	Cat# D22910
MojoSort™ Buffer (5X)	Biolegend	Cat# 480017
Brilliant Stain Buffer	Thermo Fisher Scientific	Cat# 00-4409-42
DAPI Solution	Thermo Fisher Scientific	Cat# 62248
TrueBlack® Plus Lipofuscin Autofluorescence Quencher	Biotium	Cat# 23014
ProLong™ Glass Antifade Mountant	Thermo Fisher Scientific	Cat# P36984
eBioscience™ 10X RBC Lysis Buffer	Thermo Fisher Scientific	Cat# 00-4300-54
eBioscience™ CFSE	Thermo Fisher Scientific	Cat# 65-0850-84
SIINFEKL(Ovalbumin (257-264))	MERCK	Cat# S7951
Ro5-3335	Cambridge Bioscience	Cat# HY108470
Muramyl dipeptide	Cambridge Bioscience	Cat# 30866
CADD522	Cambridge Bioscience	Cat# HY107999
S3I-201	Sigma	Cat# 573102
RPMI1640	Thermo Fisher Scientific	Cat# 11875093
Dynabeads mouse T-Activator CD3/CD28	Thermo Fisher Scientific	Cat# 11452D
Mouse IL-2 Recombinant Protein	Thermo Fisher Scientific	Cat# 212-12
DPBS, no calcium, no magnesium	Thermo Fisher Scientific	Cat# 14190250
Bovine Serum Albumin (IgG-Free, Protease-Free)	Jackson Immuno Research	Cat# 001-000-162
DPBS, calcium, magnesium, glucose, pyruvate	Thermo Fisher Scientific	Cat# 14287080
Normal Goat Serum	Abcam	Cat# ab7481
Fetal Bovine Serum	Thermo Fisher Scientific	Cat# 16140071
Critical commercial assays		
LIVE/DEAD™ Fixable Aqua Dead Cell Stain Kit, for 405 nm excitation	Thermo Fisher Scientific	Cat# L34966
Neural Tissue Dissociation Kit	Miltenyi Biotec	Cat# 130-092-628
Myelin Removal Beads II	Miltenyi Biotec	Cat# 130-096-433
AO/PI Cell Viability Kit	Labtech	Cat# F23001
Multi Tissue Dissociation Kit 1	Miltenyi Biotec	Cat# 130-110-201
Chromium Next GEM Single Cell 3' Kit v3.1	10xGenomics	Cat# 1000269
Chromium Next GEM Chip G Single Cell Kit	10xGenomics	Cat# 1000127
Dual Index Kit TT Set A	10xGenomics	Cat# 1000215

(*Continued on next page*)

Continued

REAGENT or RESOURCE	SOURCE	IDENTIFIER
Chromium Next GEM Single Cell 5' Kit v2	10xGenomics	Cat# 1000265
Library Construction Kit	10xGenomics	Cat# 1000190
Chromium Single Cell Mouse TCR Amplification Kit	10xGenomics	Cat# 1000254
Chromium Next GEM Chip K Single Cell Kit	10xGenomics	Cat# 1000287
High Sensitivity DNA Kit	Agilent Technologies	Cat# 5067-4626
eBioscience™ Foxp3 / Transcription Factor Staining Buffer Set	Thermo Fisher Scientific	Cat# 00-5523-00
$CD8a^+$ T Cell Isolation Kit, mouse	Miltenyi Biotec	Cat# 130-104-075
Pierce™ BCA Protein Assay Kits	Thermo Fisher Scientific	Cat# 23225
MINI-OSMOTIC PUMP MODEL 2002	Alzet	Cat# 0000296
BRAIN INFUSION KIT 3	Alzet	Cat# 0008851
Deposited data		
scRNA-seq, scTCR-seq data of mouse spinal cord	This manuscript	GEO: GSE281205, GSE275982, GSE275570
Experimental models: Organisms/strains		
C57BL/6J mice	Charles River UK Ltd	N/A
OT-I *Rag2*$^{-/-}$ mice	Marina Botto Lab, from Charles River UK Ltd	N/A
Nkg7-cre × mT/mG bone marrow cells	Christian R. Engwerda Lab[27]	N/A
WT(C57BL/6J) bone marrow cells	Christian R. Engwerda Lab[27]	N/A
Nkg7$^{-/-}$ bone marrow cells	Christian R. Engwerda Lab[27]	N/A
Software and algorithms		
CellRanger Version 7	10xGenomics	https://www.10xgenomics.com/company
Seurat Version 4	Butler et al.[37]	https://satijalab.org/seurat/
DoubletFinder	McGinnis et al.[38]	https://github.com/chris-mcginnis-ucsf/DoubletFinder/
scRepertoire Version 1	Bioconductor	https://ncborcherding.github.io/vignettes/vignette.html
CellChat Version 2	Jin et al.[39]	https://github.com/sqjin/CellChat
GraphPad Prism Version 10	GraphPad	https://www.graphpad.com/
FlowJo Version 10	FlowJo	https://www.flowjo.com/
ImageJ Version 2	ImageJ	https://imagej.net/software/fiji/downloads
Gene Ontology Consortium	The Gene Ontology Resource	https://www.geneontology.org/
GTRD (Gene Transcription Regulation Database) v20.06	Kolmykov et al.[40]	http://gtrd20-06.biouml.org
Cluster Profiler Version 4	Bioconductor	https://guangchuangyu.github.io/software/clusterProfiler/documentation/

EXPERIMENTAL MODEL AND STUDY PARTICIPANT DETAILS

Mice

Wild-type (WT) C57BL/6J young (8-10 weeks old) and aged (20-22 months old) mice were obtained from Charles River. OT-I *Rag2*$^{-/-}$ mice on a C57BL/6 genetic background were originally purchased from Charles River by Prof. Marina Botto (Department of Immunology and Inflammation, Imperial College London, London, UK) and transferred to us. *Nkg7*$^{-/-}$ bone marrow and *Nkg7*-cre × mT/mG bone marrow from mice on a C57BL/6 genetic background were donated by Prof. Christian R. Engwerda[27] (QIMR Berghofer Medical Research Institute, Brisbane, Queensland, Australia). All mice were housed under standard conditions at 22°C with 40%–60% humidity under a 12-h light/dark cycle and given standard chow and water ad libitum. Both male and female mice were used in an approximately equal number for each experiment. Littermates of the same sex were randomly assigned to experimental groups. No sex-dependent effect was observed. All animal procedures were performed in accordance with the UK Animals Scientific Procedures Act (1986) and approved by the ethical committee of Imperial College London.

Human material

Formalin-fixed paraffin-embedded (FFPE) tissue sections of the human spinal cord were provided by the International Spinal Cord Injury Biobank (ISCIB), University of British Columbia, Canada, and the UNITE Brain Bank, Boston, United States. The non-injured groups consisted of 17-40 years old and 41-99 years old male subjects chosen based on tissue availability and complete neuropathological reports without the presence of CNS disease. For the SCI group, aged subjects (60-87 years old) with complete spinal cord injury (ASIA impairment scale score: Grade A) were selected. Cross-sections of the spinal cord within 3 mm from the epicenter of the injury site were used for immunostaining. For the injured human spinal cord tissue sections, the biological samples transfer agreement was provided by the University of British Columbia and Vancouver Coastal Health Authority in British Columbia. Ethical approval for using the injured human spinal cord tissue sections was provided by the Imperial College Research Ethics Committee. Ethical approval for naive spinal cord tissue sections was provided by the university and hospital institutional review boards at Boston University.

METHOD DETAILS

Spinal cord injury

Surgeries were performed as previously described.[41,42] In brief, mice were subcutaneously injected with 5 mg/kg Rimadyl and 0.1 mg/kg Buprenorphine for analgesia and then anesthetized with 2.5% isoflurane in 1 L/min oxygen. Following a T9-T10 laminectomy, a dorsal hemisection until the central canal with a micro-blade or a dorsal crush (1.0 mm depth, 30 s) with a No. 5 forceps (Fine Scientific Tools) was performed bilaterally. Wet food and drinking water with Rimadyl were supplied for pain relief for 3 days. Bladders were squeezed manually to empty urine twice per day.

Axonal tracing

For corticospinal tracing, 14 days before perfusion, a craniotomy was performed to expose the right sensorimotor cortex using a micro-drill, 10% biotinylated dextran amines (BDA, D3312, Thermo Fisher Scientific) were injected into the cortex at six sites (200 nl per site). The following coordinates were used: posterior to bregma: 0.1 mm, 0.6 mm, 1.1 mm; lateral: 1.0 mm, 1.4 mm; depth: 0.7 mm as described previously.[41]

For label dorsal column (DC) axons, 7 days before sacrificing the mice, 2 μl of 15% dextran (Alexa Fluor 488-conjugated, D22910, Thermo Fisher Scientific) were injected on each side of the sciatic nerve using a 10 μl Hamilton syringe and Hamilton needle as described previously.[43]

Tissue dissociation

To prepare the cell suspension for 3' 10X genomic single cell RNA sequencing, mice were anesthetized (80 mg of ketamine and 10 mg of xylazine per kilogram of body weight via i.p. injection) and transcardially perfused with 20 ml of oxygenated cold artificial cerebrospinal fluid (CSF) solution (93 mM NMDG, 2.5 mM KCl, 1.2 mM NaH_2PO_4, 30 mM $NaHCO_3$, 20mM HEPES, 25mM glucose, 5 mM Sodium Ascorbate, 2 mM Thiourea, 0.5 mM $CaCl_2$, and 10 mM $MgSO_4$). 2mm spinal cord including the lesion site or the corresponding location in the naive spinal cord segment was immediately dissected. After, spinal cord tissues were processed using the Neural Tissue Dissociation Kit (Miltenyi Biotec, 130-092-628) following the manufacturer's protocol combined with some modifications as described previously.[10] The dissociated cells were incubated with 20ul of myelin removal beads (Miltenyi Biotec, 130-096-433) to remove myelin debris following the manufacturer's protocol. After centrifugation, cell pellets were resuspended in 1X PBS (Thermo Fisher Scientific, 14190250) + 0.04%BSA (Jackson Immuno Research, 001-000-162). An aliquot of cells was stained with Acridine Orange/Propidium Iodide dye (AO/PI Cell Viability Kit, Labtech, F23001). Cell concentration and viability were measured using the LUNA-FL Dual Fluorescence Cell Counter (Logos, L20001-LG). Cells were immediately proceeded to the 10X single cell RNA sequencing procedures.

To prepare dissociated cells for 5' 10X TCR single cell RNA sequencing, we used a very similar protocol for tissue dissection and dissociation as described above with some modifications. Especially, after anesthesia, mice were transcardially perfused with cold 1XPBS (Thermo Fisher Scientific, 14287080) and 4mm of either naive or injured spinal cord segment was dissected and further processed with enzyme digestion followed by myelin removal steps. To perverse the epitopes of T cells, the Multi Tissue Dissociation Kit 1(Miltenyi Biotec, 130-110-201) was used for tissue digestion. 40 μl of myelin removal beads were used for each sample. After myelin removal, cells were processed to the flow cytometry staining procedures before FACS.

Cell sorting

Both $CD8^+$ and $CD4^+$ T cells were sorted for TCR single cell RNA sequencing. After centrifugation of the final step in the myelin removal procedures, cell pellets were resuspended in 50 μl 1X MojoSort Buffer (Biolegend, 480017) and 0.5 μl of TruStain FcX PLUS anti-mouse CD16/32 antibody (Biolegend, 156604) was added to the cell suspension to block Fc receptors for 10 min on ice. Antibody cocktails were prepared in 50 μl Brilliant Stain Buffer (Thermo Fisher Scientific, 00-4409-42). Antibodies used for sorting were: APC anti-CD45 (30-F11, 2 μg/ml, 103111, Biolegend), Brilliant Violet 711 anti-CD8a (53-6.7, 2 μg/ml, 100759, Biolegend), Brilliant Violet 605 anti-CD4 (RM4-5, 2 μg/ml, 100547, Biolegend), FITC anti-TCR β (H57-597, 5 μg/ml, 109205, Biolegend) and LIVE/DEAD™ Fixable Aqua Dead Cell Stain Kit (Thermo Fisher Scientific, L34966, 1:1000). Cells were stained with the antibody cocktails

in the dark at 4°C for 20 min followed by two times washing with 1X MojoSort Buffer. Cell sorting was conducted using BD FACSAria III flow cytometer. After FACS, cells were washed twice with 1XPBS+0.04%BSA and immediately proceeded to the 10X TCR single cell RNA sequencing procedures.

Single-cell RNA-seq data analysis

After cell concentration measurement, 17,000 cells from each sample were loaded and processed for the library construction using the 10X Genomics Chromium Next GEM Single Cell 3' Reagent Kits v3.1 (Dual Index) according to the manufacturer's user guide. The quality of the libraries was measured using the Agilent 2100 expert High Sensitivity DNA Assay. Libraries were sequenced using a NovaSeq™ 6000 v1.5 or HiSeq 4000 sequencer. The sequencing depth was 50,000 read pairs per cell. After sequencing, raw data was processed and FASTQ files were generated using the CellRanger mkfastq pipeline. Reads were mapped to the Mouse GrCm39 genome using Cell Ranger v.7.1.0. Seurat packages were used for further analysis including quality control, integration, clustering, visualization, and differential gene expression.

Quality control

Cells with the number of RNA counts less than 750, number of genes less than 500 and percentage of mitochondrial genes more than 10% were excluded. Genes that were expressed in less than 10 cells were removed. After removing low quality cells, the DoubletFinder package was used to remove doublets, and 7.5% multiple rates were chosen as the threshold.

Integration, clustering and visualization

After doublets removal, Seurat objects were integrated using the RPCA-based integration method. SCtransform v2 normalization was applied with regressing out the variation due to mitochondrial expression. 30 principal components were selected for cell clustering. UMAP was used for the cluster visualization with a resolution of 0.3. Marker gene lists of each cluster were created by performing the FindMarkers function. Cell types were identified by using the marker genes from the literatures.

TCR single-cell RNA-seq data analysis

Sorted $CD8^+$ and $CD4^+$ T cells were processed immediately for both the single cell 5′ gene expression and V(D)J libraries construction following the 10X Genomics Chromium Next GEM Single Cell 5' Reagent Kits v2 (Dual Index) to manufacturer's user guide. Libraries were sequenced using a NovaSeq™ 6000 v1.5 sequencer. After sequencing, the FASTQs were generated using the CellRanger mkfastq pipeline. Then, the CellRanger multi pipeline was used to create the expression matrix for the 5' gene expression and the single cell V(D)J sequences and clonotypes. Reads from 5' gene expression and V(D)J libraries were mapped to the mouse mm10 genome and vdj-GRCm38 references respectively (available from 10X Genomics). The 5' gene expression matrix was used for quality control analysis using Seurat packages. In brief, low quality cells and rarely expressed genes were excluded using the same cutoffs as the 3' single-cell RNA-seq methods as described above. After removing low quality cells, the DoubletFinder package was used to remove doublets, multiple rates were chosen based on the cell numbers of each sample after cell sorting. The same methods and parameters were applied for the integration, normalization and visualization as the 3' single-cell RNA-seq. scRepertoire package was used to combine the filtered contigs from each sample and clonotypes were determined more stringently by grouping all cells that share the same VDJC genes and CDR3 nucleotide sequence. Then the clonality was integrated into the Seurat 5' gene expression metadata for the downstream analysis.

Bioinformatic analysis

Cell chat (https://github.com/jinworks/CellChat) was used for cell-cell communication analysis. GO analysis was performed using the Gene Ontology Consortium (https://www.geneontology.org/) or the Cluster Profiler R package.

Intra-spinal cord injection of SIINFEKL

Seven days after a T9-T10 spinal cord dorsal crush on OT-I *Rag2*$^{-/-}$ mice, animals were anesthetized with 2.5% isoflurane in 1 L/min oxygen and the spinal cords with injury site were exposed after reopening the sutured wound. The connective tissue around the injury site was gently cleaned and T7-T12 vertebrae were clamped with a pair of mouse spinal adaptors (World Precision Instruments (WPI)) mounted on a stereotaxic frame (WPI). 1 μl of PBS or PBS with 10 ng SIINFEKL (S7951, Merck) was delivered (50 nl/min) into the lesion core of the spinal cord in 0.5 mm depth using a sterile glass needle with a pair of laser-cut spots (diameter: 20 μm) 200 μm distance from the tip of the needle. The muscles and the skin were sutured respectively after injection and mice were transferred to the home cage when they were fully awake followed by daily monitoring.

Intracerebroventricular (ICV) antibody delivery with minipumps

To adequately deplete $CD8^+$ T cells or neutralize CXCL16 in the spinal cord, an antagonist of CD8 or CXCL16 was delivered directly into the cerebrospinal fluid (CSF) through the brain ventricle 1 h after spinal cord injury using an osmotic minipump to circumvent the brain spinal cord barrier (BSB). In brief, the preparation of pumps including drug loading and assembly with infusion sets was performed in a cell culture hood to maintain sterility. Antibodies diluted in the sterile saline at an appropriate concentration were filled into the pumps (Model 2002, Alzet) slowly without inducing any bubbles. For $CD8^+$ T cell depletion, a dosage of 50 μg of control rat IgG2b (LTF-2, BE0090, BioXcell) or rat anti-CD8a (YTS 169.4, BE0117, BioXcell) per day was applied. For neutralizing CXCL16, the dosage of control rat IgG2a (2A3, BE0089, BioXcell) or rat anti-CXCL16 (142417, MAB503, Bio-techne) was 30 μg per day. The uncapped flow

modulator was inserted into the pump and connected to a 4 cm tubing. The assembly of the pump was completed by connecting a cannula (Brain Infusion Kit 3, Alzet) to the other end of the tubing and the pumps were primed in the sterile saline at 37°C overnight. The primed pumps were implanted on the second day after spinal cord injury. The heads of anesthetized mice were fixed on a stereotaxic frame (WPI) using ear and nose holders. An incision was made in the skin above the skull from the neck to up in between the eyes. The pumps were inserted under the skin at the neck and pushed back toward the left hindlimb. A single drop of super glue was placed on the base of the cannula which was then pushed into the cannula driver (Alzet) on the stereotaxic frame. The cannula was moved to the position where the catheter tip was touched to bregma to zero the coordinates. The catheter was then raised and moved 1.1 mm laterally to the right and 0.5 mm posterior. The catheter was driven down through the skull until the cannula base was completely pressed against the top of the skull and was held for 2 min to dry the glue. The top of the cannula was clipped off with a bone clipper (Fine Scientific Tools) from the groove and the skin was then sutured. For the chronic SCI experiment, the pumps were changed every 14 days and removed at day 70 after implantation.

Delivery of antibodies via intraperitoneal injection

To deplete $CD8^+$ T cells *in vivo* for the axonal regeneration and single cell RNAseq experiments, 200 μg of anti-mouse CD8α (YTS 169.4, BioXcell, BE0117) or rat IgG2b (LTF-2, BioXcell, BE0090) was i.p. injected into the old mice 4 h after spinal cord injury. The injections were performed twice per week for 4 weeks or 10 weeks.

Immunohistochemistry

Mice were anesthetized (80 mg of ketamine and 10 mg of xylazine per kilogram of body weight via i.p. injection) and transcardially perfused with 20 ml of ice-cold 1X PBS (pH 7.4) followed by 20 ml ice-cold 4% paraformaldehyde (PFA) (Sigma) in 1X PBS. Spinal cords were dissected and post-fixed in 4% PFA overnight at 4°C followed by an immersion in 30% sucrose (Sigma) for 5 days. Thereafter, spinal cords were embedded in an OCT compound (Leica) and sectioned at 20 μm thickness. Sections were washed with 1X PBST three times and treated with a blocking solution containing 10% normal goat serum (ab7481, Abcam) and 0.3% Triton X-100 in PBS for 1 h at room temperature and then incubated with primary antibodies at 4°C overnight. The primary antibodies include: chicken anti-GFAP (1:500, ab4674, Abcam); rat anti-CD31 (1:100, 550274, BD Biosciences); rabbit anti-CD8 (1:200, ab217344, Abcam); rat anti-Iba1 (1:5000, ab283346, Abcam); mouse anti-Granzyme K (1:100, 67272-1-Ig, Proteintech); rat anti-MHC-I (1:100, NB100-64952, Novus); rabbit anti-Collagen I (1:200, ab21286, Abcam); rabbit anti-CD3 (1:200, ab16669, abcam); rabbit anti-Fibronectin (1:500, AB2033, Millipore); rabbit anti-Iba1 (1:500, ab178846, Abcam); Rabbit anti-phospho-Stat3 (1:200, #9145, Cell Signaling Technology). Sections were washed with 1X PBST three times and stained with goat secondary antibodies (Thermo Fisher Scientific) at room temperature for 2 h. DAPI (Thermo Fisher Scientific, 62248, 0.2 μg/ml) was costained with secondary antibodies. After washing with 1X PBS, sections were incubated with TrueBlack Plus solution (1:40 in PBS, 23014, Biotium) for 10 min followed by three washes with 1XPBS and then mounted with ProLong™ Glass Antifade Mountant (Thermo Fisher Scientific, P36984). Sections were imaged with a Leica TCS SP8 confocal laser scanning microscope in the Leica DFC9000 GTC detection system.

Injured human spinal cord sections were initially treated with Xylene (Sigma) two times for 10 min each for deparaffinization and rehydrated in a series of graded ethanol (100%: two times for 10 min each, 95%: two times for 5 min each, 70%: two times for 5 min each, and 50%: one time for 5 min respectively). Sections were rinsed with deionized water and incubated with 1X PBS for 10 min. After, sections were immersed in boiled Tris-EDTA buffer (10 mM Tris base, 1 mM EDTA solution, 0.05% Tween 20, pH 9.0) for 10 min to retrieve the epitope. Continue with the blocking step and staining protocol as described above. The primary antibodies used were: chicken anti-GFAP (1:500, NBP1-05198, Novus); rabbit anti-CD8 (1:200, ab237709; Abcam); mouse anti-Granzyme K (1:100, 67272-1-Ig, Proteintech); mouse anti-NKG7 (1:100, GTX01839, GeneTex). Sections were imaged with a Zeiss Axio Observer microscope.

Naive human spinal cord section immunostaining was performed following a similar protocol. Slides were digitally imaged using a Perkin Elmer Vectra Polaris slide scanner (Akoya Biosciences, Marlborough, MA) at 20X magnification.

Image analysis

Arbitrary fluorescent intensity was measured with ImageJ (Fiji) software (National Institute of Health, USA) and normalized by subtracting the intensity of the background signal. The cells designated positive for the expression of targets showed fluorescence intensity at least 2-fold above the background. For axonal quantification, an inter-animal comparable ratio was obtained by normalizing the number of labelled axons at each distance to the total number of labelled axons at 1 mm rostral (for CST) or caudal (for DC) to the lesion border. The total length of 5-HT fibers was measured using the NeurphologyJ plugin in ImageJ. The ramification of $Iba1^+$ cells was analysed using the ImageJ plugin AnalyzeSkeleton (2D/3D) as described elsewhere.[44]

For naive human spinal cord images, immunofluorescent slides were spectrally unmixed through Phenochart and InForm Image Analysis software (Akoya Biosciences, Marlborough, MA) to remove autofluorescence. HALO (Indica Labs, Albuquerque, NM) software was used to quantify cell densities and provide image reconstructions. Two ROIs of the spinal cord were annotated including the grey matter (GM) and white matter (WM). The total number of $CD8^+$ T cells was quantified in both ROIs and reported as cell densities. On average three cervical level of human spinal cord sections were examined per individual for young versus aged analyses. The traced regions of interest excluded any meningeal tissue. To determine localization, we assessed the proportion of T cells that

were perivascular, or residing near blood vessels, and parenchymal defined as those that were beyond 30 μm of a CD31$^+$ endothelium. This distance was based on the average radius of the perivascular space in our samples.

Flow cytometry

To characterize cells *in vivo*, mice were anesthetized (80 mg of ketamine and 10 mg of xylazine per kilogram of body weight via i.p. injection) and transcardially perfused with 20 ml of ice-cold PBS and a 4 mm truncated spinal cord with or without injury site from naive or spinal cord injured mice was dissected and enzymatically dissociated using Multi Tissue Dissociation Kit 1(Miltenyi Biotec, 130-110-201). Myelin debris was cleaned from the cell suspensions by using myelin removal beads (Miltenyi Biotec, 130-096-433). After centrifugation, cell pallets were then resuspended with 50 μl 1X MojoSort Buffer (Biolegend, 480017) and treated with 0.25 μg of TruStain FcX PLUS anti-mouse CD16/32 antibody (Biolegend, 156604) per sample for 10 min on ice. Then, cells were stained with a cocktail of fluorescence-conjugated antibodies prepared in 50 μl Brilliant Stain Buffer (Thermo Fisher Scientific, 00-4409-42) for 20 min at 4°C in the dark. The following anti-mouse antibodies were used: PE/Cyanine5 anti-mouse CD45 Antibody (30-F11, 2 μg/ml, 103110, Biolegend), Brilliant Violet 711™ anti-mouse CD8a Antibody (53-6.7, 2 μg/ml, 100759, Biolegend), Brilliant Violet 605™ anti-mouse TCR β chain Antibody (H57-597, 2 μg/ml, 109241, Biolegend), Brilliant Violet 785™ anti-mouse/human CD11b Antibody (M1/70, 2 μg/ml, 101243, Biolegend), APC/Fire™ 750 anti-mouse CD4 Antibody (RM4-5, 2 μg/ml, 100568, Biolegend), FITC anti-mouse CD186 (CXCR6) Antibody (SA051D1, 2 μg/ml, 151107, Biolegend), APC/Cyanine7 anti-mouse CD69 Antibody (H1.2F3, 2 μg/ml, 104525, Biolegend), FITC anti-mouse TCR γ/δ Antibody (GL3, 5 μg/ml, 118105, Biolegend), PE/Cyanine7 anti-mouse NK-1.1 Antibody (S17016D, 2 μg/ml, 156513, Biolegend). LIVE/DEAD Fixable Aqua Dead Cell Stain Kit (Thermo Fisher Scientific, L34966, 1:1000) was used to identify live and dead cells from staining. For intracellular staining, cells stained with antibodies against cell surface molecules were washed with flow cytometry staining buffer and fixed/permeabilized with the Foxp3/Transcription Factor Staining Buffer Set (Thermo Fisher Scientific, 00-5523-00). After cell fixation and permeabilization, samples were stained with PE anti-TIA-1(NKG7) antibody (2G9A10F5, 1:100, IM3293, Beckman Coulter) for 30 min at room temperature and protected from light. Cells were then washed with 1X permeabilization buffer and resuspended in an appropriate volume of 1X MojoSort Buffer for further acquisition using a 5-laser BD FACSymphony A3 Cell Analyzer, then data were analyzed on FlowJo version 10.

Total cell numbers were counted with flow cytometry by running out the whole sample prepared from the same size of spinal cord between individuals. 10,000 blood or bone marrow CD45$^+$ cells of each sample were acquired for quantification. Full stain minus one (FMO)-NKG7, FMO-NK1.1, FMO-TCRγδ, and FMO-SIINFEKL controls were used to discriminate the positive from the negative cells.

Adoptive cell transfer

To investigate the correlation of NKG7 expression and CD8$^+$ T cell proliferation, splenocytes from OT-I *Rag2*$^{-/-}$ mice were extracted following lysis of erythrocytes using RBC Lysis Buffer (00-4300-54, Thermo Fisher Scientific). CD8$^+$ T cells were purified by the negative selection method with a CD8a$^+$ T Cell Isolation Kit (130-104-075, Miltenyi Biotec). CD8$^+$ T cells were washed two times with PBS to remove any serum and resuspended at 1 x 10^7/mL of PBS. Carboxyfluorescein succinimidyl ester (CFSE, 65-0850-84, Thermo Fisher Scientific) was added to the final concentration of 5 μM per ml of cells for 20-min incubation at room temperature in the dark. Five volumes of cold complete media RPMI1640 (Thermo Fisher Scientific, 11875093) + 10% FBS (16140071, Thermo Fisher Scientific)) was added to stop labelling and incubated on ice for 5 min. After three times wash with complete media, CFSE-labelled CD8$^+$ T cells were suspended with complete media and 10 million cells in 200 μl saline were intravenously injected into each WT recipient. Twenty-four hours later, 50 μg SIINFEKL was delivered to each recipient by intraperitoneal injection and the spleens of the recipients were dissected 48 h after SIINFEKL stimulation for cell staining and flow cytometry analysis.

Bone marrow chimeras

Three-month-old WT or *Nkg7*$^{-/-}$ mice were sacrificed, and the femurs were dissected. After the muscle was cleaned, bone marrow was flushed out with sterile PBS using a 27-gauge needle and syringe. Bone marrow was passed through a 22-gauge needle to break up the clumps and the cell suspension went through a 40 μm cell strainer to remove the large fragments. Before irradiation, drinking water containing 0.01% Baytril (Enrofloxacin) was supplied to 18-month-old WT mice (recipients) for 1 week. For irradiation, the recipients were placed in a container (2 mice at a time) and irradiated to deliver a dosage of 15 Gy (two times 7.5 Gy, 2 h between each irradiation). Four hours after the second irradiation, ten million WT or *Nkg7*$^{-/-}$ bone marrow cells were intravenously injected into each recipient. Drinking water with Enrofloxacin was supplied for 1 month after irradiation to prevent the mice from infection. Blood samples from the recipients' tail veins were collected every month after irradiation for bone marrow reconstitution measurement by flow cytometry. Aged *Nkg7*-cre × mT/mG bone marrow chimeras were also generated following the same procedure above.

Transcription factor screening

GTRD (Gene Transcription Regulation Database): http://gtrd20-06.biouml.org was used to identify transcription factor that are involved in *Nkg7* expression.

To identify the transcription factors of *Nkg7* in CD8$^+$ T cells *in vitro*, primary CD8$^+$ T cells were isolated from spleens of WT mice using a CD8a$^+$ T Cell Isolation Kit (130-104-075, Miltenyi Biotec and expanded with mouse T-Activator CD3/CD28 Dynabeads (11452D, Thermofisher) and 30 U/mL mouse IL-2 recombinant protein (212-12, Thermofisher) for 5 days. 8 X 10^4 CD8$^+$ T cells per

well with 2 μL Dynabeads in 96-well plate were plated. Vehicle (0.1% DMSO in culture medium), 25 μM Ro5-3335 (HY108470, Cambridge Bioscience), 10 μg/mL Muramyl dipeptide (MDP, 30866, Cambridge Bioscience), 50 μM CADD522 (HY107999, Cambridge Bioscience) or 10 μM S3I-201 (573102, Sigma) was added in each well after plating the cells.

After 5-day cell culture, cells were suspended and transferred to a new Eppendorf tube and placed on a magnetic rack for 1 min to remove the dynabeads. Cells were transferred to a new tube and washed with cold PBS for 3 times and used for qPCR.

To investigate the effects of STAT3 inhibition on *Nkg7* expression *in vivo*, spinal cord dorsal hemi-crush injury was performed on the aged *Nkg7*-cre × mT/mG bone marrow chimeras, after, vehicle or 2.5 mg/kg SI3-201 was i.p. injected 3 times per week for 1 week followed by mouse sacrifice and tissue dissection for further analysis.

Immunoblotting

$CD8^+$ T cell purified from the blood of the aged *Nkg7*-cre × mT/mG bone marrow chimeras were collected 1 week after injury followed by vehicle or STAT3 inhibitor delivery. Protein lysate was extracted by RIPA buffer with protease and phosphatase inhibitors (Roche). Protein concentration was measured with BCA protein assay kit (ThermoFisher) and 20 μg of protein was loaded to 10% SDS-PAGE gel and transferred on nitrocellulose membrane of iBlot Transfer Stack (ThermoFisher) by iBlot 2 Gel Transfer Device (ThermoFisher) under the default P0 program. The membrane was blocked with 5% BSA (Sigma) in TBST buffer for 1 h at RT and incubated with primary antibodies: anti-phospho-Stat3 (1:1000, #9145, Cell Signaling Technology), anti-Stat3 (1:1000, #9139, Cell Signaling Technology), anti-GAPDH (1:1000, #2118, Cell Signaling Technology) at 4°C overnight. The membranes were then washed with TBST and incubated with Horseradish peroxidase (HRP)-conjugated secondary antibodies at RT for 1 h followed by the chemiluminescent detection with Amersham Hyperfilm (GE Healthcare Life Sciences) after the incubation with ECL substrate (ThermoFisher).

Real-time PCR for *Nkg7* expression analysis

Total RNA from cultured $CD8^+$ T cells was extracted using RNeasy kit (Qiagen) according to manufacturer's guidelines. cDNA was then synthesized with SuperScript II Reverse Transcriptase (ThermoFisher). qRT-PCR was performed using KAPA SYBR® FAST qPCR kit (Sigma, KK4601) from QuantStudio 3 (Thermofisher) Real-Time PCR System. Ct values normalized versus Gapdh as a housekeeping gene were exported and relative fold change of gene expression compared to vehicle control was calculated by $2^{-\Delta\Delta Ct}$. Primers used in qPCR were as follows: *Nkg7* forward 5′- TCAAGTCCAGACATTCTTCTCCT-3′ and reverse 5′- CACAAGGTTTCATACTCAGCCC-3′, *Gapdh* forward 5′-TCAACAGCAACTCCCACTCTTCCA-3′ and reverse 5′-ACCCTGTTGCTGTAGCCGTATTCA-3′.

Behavioral assessments

Mice were gently handled daily for 7 days and then acclimatized to the Basso Mouse Scale with an open field and to the grid walk instrument every day for 7 days. The investigators who participated in the behavioral scoring were blinded to the groups and treatments. Mice that underwent spinal cord injury and minipump implantation were tested every week for 10 weeks in total after injury.

Basso Mouse Scale (BMS)

The BMS assessment was performed as previously described.[41] Briefly, two experienced examiners evaluated the motor behavior of each mouse in terms of ankle movement, paw placement, stepping, coordination etc. following the BMS instruction on the open field for 5 min and assigned a defined score for each hindlimb.

Grid walk

The grid walk consists of a 50 cm X 3 cm metal grid bridge placed between two wood blocks with 40 cm height. Each grid was formed by 1 cm X 1cm spaces. Animals with the BMS score $\geq$ 4 (stepping) were assessed on the grid walk. Mice were video recorded for six runs of the entire grid length in both directions and the number of missteps were counted.

QUANTIFICATION AND STATISTICAL ANALYSIS

All statistical analyses were performed using GraphPad Prism software. All values are presented as the mean ± SEM. Statistical comparisons included the two-tailed unpaired t test with Welch's correction, two-tailed Pearson's correlation test, one-way or two-way ANOVA followed by Sidak's, Tukey's, or Bonferroni's multiple-comparisons post hoc tests as specified in the figure legends. The exact value of *n* and what *n* represents can be found in the figure legends.

No methods were used to determine whether the data met assumptions of the statistical approach.